AFRL-PR-WP-TR-2006-2099

THERMAL MANAGEMENT OF NEXT-GENERATION POWER ELECTRONICS FOR THE MORE-ELECTRIC AIRCRAFT INITIATIVE

Dr. Scott K. Thomas
Andrew J. Fleming

Wright State University
Department of Mechanical and Materials Engineering
3640 Colonel Glenn Hwy.
Dayton, OH 45435-0001

JULY 2005

Interim Report for 12 July 2004 – 12 July 2005

Approved for public release; distribution is unlimited.

STINFO COPY

PROPULSION DIRECTORATE
AIR FORCE MATERIEL COMMAND
AIR FORCE RESEARCH LABORATORY
WRIGHT-PATTERSON AIR FORCE BASE, OH 45433-7251

NOTICE

PAO case number: AFRL/WS 06-0271
Date cleared: 02 FEB 2006

THIS TECHNICAL REPORT IS APPROVED FOR PUBLICATION.

//Signature//	//Signature//
KIRK L. YERKES, PhD	JOHN G. NAIRUS
Deputy for Science	Chief
Power Division	Electrochemistry and Thermal Sciences Branch

REPORT DOCUMENTATION PAGE

Form Approved
OMB No. 0704-0188

1. REPORT DATE *(DD-MM-YY)*	2. REPORT TYPE	3. DATES COVERED *(From - To)*
July 2005	Interim	07/12/2004 – 07/12/2005

4. TITLE AND SUBTITLE
THERMAL MANAGEMENT OF NEXT-GENERATION POWER ELECTRONICS FOR THE MORE-ELECTRIC AIRCRAFT INITIATIVE

5a. CONTRACT NUMBER
In-house

5b. GRANT NUMBER

5c. PROGRAM ELEMENT NUMBER
62203F

6. AUTHOR(S)
Dr. Scott K. Thomas
Andrew J. Fleming

5d. PROJECT NUMBER
3145

5e. TASK NUMBER
20

5f. WORK UNIT NUMBER
C9

7. PERFORMING ORGANIZATION NAME(S) AND ADDRESS(ES)
Wright State University
Department of Mechanical and Materials Engineering
3640 Colonel Glenn Hwy.
Dayton, OH 45435-0001

8. PERFORMING ORGANIZATION REPORT NUMBER

9. SPONSORING/MONITORING AGENCY NAME(S) AND ADDRESS(ES)
Propulsion Directorate
Air Force Research Laboratory
Air Force Materiel Command
Wright-Patterson AFB, OH 45433-7251

10. SPONSORING/MONITORING AGENCY ACRONYM(S)
AFRL-PR-WP

11. SPONSORING/MONITORING AGENCY REPORT NUMBER(S)
AFRL-PR-WP-TR-2006-2099

12. DISTRIBUTION/AVAILABILITY STATEMENT
Approved for public release; distribution is unlimited.

13. SUPPLEMENTARY NOTES
Report contains color.

14. ABSTRACT

The objective of this project is to determine the suitability of using a loop heat pipe with water as the working fluid as a method of dissipating heat from electronics onboard aircraft. This will be accomplished by designing an experimental apparatus to be mounted to the centrifuge table test bed in Bldg. 71B in Wright-Patterson Air Force Base. The experiment will consist of a high-temperature fluid loop, and an analysis of the heat transfer from a heated plate at zero angle of attack as a function of the altitude and speed of the aircraft, and the atmospheric weather conditions. In addition, the future directions of the project are outlined.

15. SUBJECT TERMS
Aircraft actuator thermal management, loop heat pipe, centrifuge table, increased body forces

16. SECURITY CLASSIFICATION OF:			17. LIMITATION OF ABSTRACT:	18. NUMBER OF PAGES	19a. NAME OF RESPONSIBLE PERSON (Monitor)
a. REPORT	b. ABSTRACT	c. THIS PAGE			Dr. Kirk L. Yerkes
Unclassified	Unclassified	Unclassified	SAR	92	19b. TELEPHONE NUMBER *(Include Area Code)* (937) 656-4428

Standard Form 298 (Rev. 8-98)
Prescribed by ANSI Std. Z39-18

Table of Contents

List of Figures

List of Tables

Nomenclature

a	Speed of sound, m/s; acceleration, m/s^2
a^+	a/g, acceleration normalized to gravity
A	Area, m^2
B	Experimental constant related to Eq. (1.2)
$C^*_{f,L}$	Local skin friction coefficient evaluated at the end of the plate
c_p	Specific heat, J/(kg-K)
g	Acceleration due to gravity, m/s^2
h_L	Local heat transfer coefficient at the end of the plate, W/(m^2-K)
$\overline{h}$	Overall heat transfer coefficient, W/(m^2-K)
H	Altitude, m
k	Thermal conductivity, W/(m-K)
L	Plate length, m
Ma	Mach number
Pr	Prandtl number
q_x	Heat rate generated by the electronics package, W
q''_w	Average heat flux dissipated from the plate, W/m^2
r	Recovery factor; radial coordinate, m
R	Particular gas constant, m^2/(s^2-K), or thermal resistance, K/W
R^2	Coefficient of determination
R''_c	Contact thermal resistance per unit area of the interface, m^2-K/W
Re_L	Reynolds number evaluated at the end of the plate
St_L	Local Stanton number evaluated at the end of the plate
t	Thickness, m
T	Temperature, K
T_{aw}	Adiabatic wall temperature, K
T_w	Wall temperature, K
U	Velocity, m/s
V	Voltage, V
z	Axial coordinate
γ	Ratio of specific heats
ΔT	Temperature difference, K
θ	Azimuthal coordinate
μ	Absolute viscosity, (N-s)/m^2
ρ	Density, kg/m^3

Superscript

*	Film condition
+	Normalized

Subscripts

∞	Freestream condition

aw	Adiabatic wall
ct	Centrifuge table
hs	Heat spreader
max	Maximum value
r	Radial
R	Reference condition
s	Aircraft skin
Z	Axial
θ	Azimuthal

Introduction

The objective of this project is to determine the suitability of using a loop heat pipe with water as the working fluid as a method of dissipating heat from electronics onboard aircraft. This will be accomplished by designing an experimental apparatus to be mounted to the centrifuge table test bed in Bldg. 71 in Wright-Patterson Air Force Base. The experiment will consist of a high-temperature fluid loop, a low-temperature fluid loop, various sensors, and an upgraded data acquisition system. This interim report describes the current status of the project, which includes the new data acquisition system, an initial design of the high-temperature fluid loop, and an analysis of the heat transfer from a heated plate at zero angle of attack as a function of the altitude and speed of the aircraft, and the atmospheric weather conditions. In addition, the future directions of the project are outlined.

Chapter 1: Aircraft Thermal Management using Loop Heat Pipes: Experimental Simulation of High Acceleration Environments using the Centrifuge Table Test Bed

1.1 Centrifuge Table Upgrade

The aircraft environmental acceleration test bed consists of an 8-ft.-diameter centrifuge table used to evaluate potential thermal management concepts for high performance aircraft. Initial testing has shown acceleration capabilities greater than 12 g and maximum onsets of 11 g/s with generated noise on the order of 10^{-5} g. The previous centrifuge table data acquisition system dated back to the early 1990's. The original computer was a Pentium 386 running ViewDAC for data collection and reduction. At the start of this project, it was determined that the data acquisition system needed to be upgraded, including the data acquisition unit and computer system. Since all of this equipment was going to be upgraded, it was decided to completely evaluate the existing data acquisition wiring and document this information.

1.2 Updating the Centrifuge Table Wiring and Documentation

The first step to updating the data acquisition system was to record the original data acquisition wiring. All of the wiring on the centrifuge table was rewired and documented so that it would be easier to trace wiring back to the centrifuge table control room. The wiring scheme on the centrifuge table can be seen in Figure 1.1. The terminal strip at the bottom of this photo is located on the rotating table, while the terminal strips at the top are on the stationary support. These are connected via a 40-ring slip ring. A new wiring panel was developed for the wiring coming from the stationary terminal strips above the centrifuge table back to the control room, as shown in Figure 1.2. Wiring on the centrifuge table terminal strip now matches the wiring coming into the centrifuge table control room. This information was completely documented for future reference. Each circuit from the centrifuge table to the slip ring wiring panel in the control room was checked for continuity by hand.

After verifying the wiring configuration was in proper operating condition, documentation for the new data acquisition hardware was reviewed so that the upgrades

could be started. Initially, a new wiring panel was developed for the new data acquisition interface as shown in Figure 1.3. This panel was designed to accommodate 64 channels (three wires per channel) for data acquisition, as well as 16 channels (four wires per channel) for voltage and current control. Each circuit from the data acquisition interface panel to the two new data acquisition modules was checked for continuity by hand. Jumper cables were created to transfer signals coming in from the slip rings to the data acquisition wiring panel. An Excel spreadsheet was created to track the wiring from each slip ring to the data acquisition modules, as shown in Table 1.1, as well as wiring for the D/A converter shown in, and the thermocouple filter board shown in .

1.3 Data Acquisition Unit

The new data acquisition system arrived in January 2005. This unit from Agilent Technologies has a mainframe (E8408A) with four slots into which the following cards were installed: a command module (E1406A), an 8/16 channel D/A converter (E1418A), a 5½-digit multimeter (E1411B), and a sixty-four channel, 3-wire multiplexer (E1476A). The command module serves as the main source of communication between all of the cards in the mainframe. The command module also exchanges data and commands between the computer and data acquisition system. The D/A converter is a control type module, allowing the user to request a certain output voltage or current from up to sixteen channels. The multimeter reads the voltages that the multiplexer collects from thermocouples, pressure transducers, accelerometers, etc., as well as any externally applied voltages, currents, and resistances. Communication between the data acquisition system and the computer takes place via the general purpose interface bus (GPIB) or IEEE-488 protocol. Essentially, text commands are sent from the computer to the data acquisition system. Then, if the command requests a control signal, the proper output is processed. If the command were for data acquisition, then ASCII data is returned to the user for processing.

1.4 Data Acquisition/Computer Communication

With the new data acquisition system and computer assembled, documentation for the data acquisition system needed to be reviewed to determine the proper commands necessary to use the computer to communicate with the data acquisition system. Initially,

single text lines were sent from the computer using Agilent's VISA Assistant software. Commands were sent to read thermocouple temperatures on one of the channels of the multiplexer.

The software used for writing the data acquisition code was LabVIEW, which is a visual computer language. LabVIEW was a new program to everyone in the branch, so learning this program started at the beginner level. After studying LabVIEW help books and performing many examples, the task of writing a simple VISA command to read a voltage was completed.

Virtual instruments (VIs) for communicating with the data acquisition system started fairly crudely. Virtual instruments are subprograms that are written with certain inputs and calculated outputs, which can greatly simplify a complicated code. First, the task of reading several voltage channels and outputting the data to the screen was accomplished. Second, the reading of several voltage channels was placed inside a timed loop such that data would be recorded at regular intervals and written to a file that Microsoft Excel could read. Next, the proper conversions for voltage to temperature, acceleration, and pressure were written into the code so that actual data was recorded to a file.

The next task to be accomplished with this software was control communication. What was desired was a system where a certain voltage could be applied to increase the angular velocity of the centrifuge table, and to control a variety of other devices, such as pumps, heaters, etc. Following a similar process to the development of the data acquisition software, a virtual instrument was written that could control the output voltage of several channels along with the capability of turning them on and off at any time. This VI was then merged with the data acquisition program with appropriate Boolean commands for control. This VI was tested and verified when data was collected for a liquid-vapor separator experiment on the centrifuge table, as shown in Figure 1.4. A program was tailored for this experiment, including the appropriate flow meter, pressure transducer, and accelerometer conversions. Data was recorded, some of which can be seen in Figure 1.5. The program worked well with only minor modifications.

Shortly after these tests it was suggested to purchase a second monitor for the data acquisition computer such that graphical output could be viewed on one monitor and

controls and raw data could be viewed on the other. This system was implemented in June 2005 and greatly increased the readability of the graphical data as well as enlarging the raw data indicators so they could be read from farther away.

After control of the centrifuge table was accomplished using a voltage from the D/A converter to control the angular velocity, it was decided to control the acceleration directly. The first attempt to control the acceleration in the form of a slider bar was to write a VI that read the acceleration from an accelerometer on the centrifuge table and compared it with the desired acceleration. Then, based on this difference, the table voltage would be increased or decreased to reach the desired acceleration. This program was effective until at higher radial acceleration levels when a second-order transient response occurred. As a result, it was suggested that a PID controller system be implemented to control the acceleration. A PID controller was coded in LabVIEW and the system turned on, but a fast enough sampling rate could not be reached to effectively implement this system. It was then determined that since the centrifuge table motor is already controlled using a PID controller, it does not make sense to try an implement another software-based PID controller. A relation was then developed between voltage and acceleration. Centrifugal acceleration is given by

$$a_r^+ = \frac{r\omega^2}{g} \tag{1.1}$$

Voltage is related to angular velocity by

$$V = B\omega \tag{1.2}$$

where B is an experimental constant to be determined. Substituting this relation into the expression for centrifugal acceleration yields

$$a_r^+ = \frac{r}{g}\left(\frac{V}{B}\right)^2 \tag{1.3}$$

Solving Eq. (1.3) for voltage yields the relation used for deriving a corresponding voltage for a chosen centrifugal acceleration.

$$V = B\sqrt{\frac{a_r^+ g}{r}} \tag{1.4}$$

Thus, voltage is linearly related to the square root of centrifugal acceleration. This relation can be extended to relate voltage and the acceleration magnitude. The magnitude of acceleration is given by

$$a^+ = \sqrt{a_\theta^{+2} + a_r^{+2} + a_z^{+2}} \tag{1.5}$$

where a_θ^+, a_r^+, and a_z^+ are the accelerations normalized by gravity in the azimuthal, radial, and axial directions on the centrifuge table. Solving for the radial acceleration gives

$$a_r^{+2} = a^{+2} - a_\theta^{+2} - a_z^{+2} \tag{1.6}$$

When the centrifuge table is rotating with a constant velocity, $a_\theta^+ = 0$ and $a_z^+ = -1$. After substituting these values in for Eq. (1.6) and solving for the square root of centrifugal acceleration

$$\sqrt{a_r^+} = \left(a^{+2} - 1\right)^{1/4} \tag{1.7}$$

Substituting Eq. (1.7) into Eq. (1.4) yields the relation between table voltage and the magnitude of the acceleration.

$$V_{ct} = B\sqrt{\frac{g}{r}}\left(a^{+2} - 1\right)^{1/4} \tag{1.8}$$

To calculate *B*, experimental data relating table voltage with centrifugal acceleration was collected. Then, a plot of voltage versus the square root of centrifugal acceleration was generated and a linear best fit regression was derived with the voltage intercept forced through the origin. The corresponding slope is then $B\sqrt{g/r}$. Since the radial location of the accelerometer is known, *B* can then be calculated. A sample plot can be seen in Figure 1.6. After the constant *B* for this equation was found, an acceleration control slide bar was added to the data acquisition program by deriving a corresponding voltage output. It is important to note that *B* is experiment specific, and if the location of the accelerometer is changed, a new value for *B* needs to be found.

The current LabVIEW data acquisition setup has many capabilities and a few limitations. The centrifuge table now has a computer-based control of the acceleration seen by an experiment mounted to the table. Any steady-state application works well using this program, along with several other voltage outputs for pumps and heaters at steady-state. Sixty-four channels of data signals can be read at once, but the system is limited by the forty channels on the slip ring. How quickly data can be acquired and processed is dependent on the number of channels that are being read. For the liquid-vapor separator experiment, ten channels were read and processed, meaning voltages were read, converted to useful data, written to a data file, and presented to the screen in graphical and raw format, in about 0.5 s. For an experiment that uses all sixty-four channels, this period can be as long as 3 s. Along with the data acquisition channels there are sixteen channels of output control signals that can be handled at once. Figure 1.7(a) shows the front panel of a virtual instrument written for the liquid-vapor separator experiment in LabVIEW for controlling voltage outputs, viewing returning data, and recording data to file. On the left side are the slider bars that control the acceleration seen on the table, both magnitude and radial, and the voltages for controlling the two liquid pumps. To the right of this are various control parameters that the user can set based on the experimental setup. In the middle of the panel is the numerical raw data output that updates in real-time. On the right side are real-time strip charts of acceleration, pressures, and volumetric flow rates. The wiring diagram in Figure 1.7(b) shows all of

the voltage controls on the left side and all the data collection and output on the right side.

Problems with this program occur when transient voltage outputs are generated. Transient control is desired to mimic what will occur on an aircraft. If an aircraft suddenly banks, a high acceleration loading will be applied to the system. Then, after a short delay, the increased heat load from the actuator will be seen by the thermal management device. This type of situation can be modeled as two sine waves that are offset from one another by a phase lag. Due to the limitations of the data acquisition system, a sinusoidal voltage output can not be properly generated. Since voltage data points can only be output at the speed of the program, what is seen on an oscilloscope is a stair-stepped version of a sine wave with a different frequency than what was desired as shown in Figure 1.8(a). Another problem with this method occurs when data is being acquired. The voltage output of the sine wave pauses such that it maintains a constant voltage while data acquisition occurs, then continues the sine wave where the program left off as shown in Figure 1.8(b). A possible solution for this problem is to introduce an arbitrary waveform generator module (E1441A) to the data acquisition system. This arbitrary waveform generator module can create the standard output signals of a function generator as well as store an arbitrary waveform in memory. This would eliminate the problem with sine waves appearing stair-stepped and at a different frequency, as well as problems when data acquisition is occurring. The cost of an arbitrary waveform generator module is $3205. To install this module would require a larger mainframe (E1421B) with six slots, which costs $4200.

Several virtual instruments (VIs) have been created for use in programming. A subVI has been written, shown in Figure 1.9, which automatically sends the text commands for data acquisition, returns the voltages, and then uses more subVIs to convert the voltages to useful data. These subVIs have been written to convert voltages to accelerations shown in Figure 1.10, pressures shown in Figure 1.11, temperatures shown in Figure 1.12, and volumetric flow rates shown in Figure 1.13. All of these VIs were then implemented in the main program that controls the centrifuge table, presents graphical output, and writes data to a file.

1.5 New Thermocouple Amplifier for the Centrifuge Table

It was desired to have the capability of reading higher temperatures on the centrifuge table. The current thermocouple amplifier on the centrifuge table is for Type T thermocouples, which have an operating temperature range between -250 to 350°C. A new Type E thermocouple amplifier has been specified and purchased with operating temperatures between -200 to 900°C. This amplifier unit will be installed on the underside of the centrifuge table opposite of the existing thermocouple amplifier so that either one can be used, depending on the experimental requirements.

1.6 Recirculating Chiller Maintenance

The recirculating chiller used in the centrifuge table test cell had not been used since the late 1990's. The chiller feeds a mixture of ethylene glycol and water to a rotary double-bypass hydraulic coupling above the centrifuge table, which in turn feeds six ports on the table for removing heat from the table while it is spinning. Over time, the ethylene glycol/water mixture had developed bacteria in the tank, lines, and filter. The tank was drained of all fluid and the bacteria were removed from inside the tank. All of the lines were drained to remove any excess fluid. The inside of the tank was then sprayed down several times with a garden hose to knock more of the bacteria out. The filter unit was completely clogged with the bacteria, so the entire unit was replaced. A mixture of Clorox and water was then placed in the tank to give the tank a thorough cleaning. This was then drained and replaced with water. Then all of the fluid lines on the table were purged by allowing water to flow out of the supply lines. The supply and drain ports were connected together to allow complete fluid flow through the system at each of the six table ports. Then the system was completely drained. This was performed twice to clear the system of impurities. Approximate flow rates were calculated using the standard pump in the recirculating chiller as well as flow rates at various booster pump settings. Data for these flow rates can be seen in Table 1.3.

During the process of cleaning the recirculating chiller, it was discovered that the chiller temperature control was not working properly. The potentiometer can be turned, and the system seems to increase or decrease the fluid temperature accordingly. The

temperature readout does not correctly display what the temperature setpoint of the system is for the given location of the potentiometer.

1.7 Design of the High-Temperature Fluid Loop for the Loop Heat Pipe Experiment

Currently in design is the high-temperature fluid loop, which will be mounted onto the centrifuge table. Figure 1.14 shows a schematic diagram of the loop, which consists of a copper cold plate, a liquid-liquid heat exchanger, a fill/purge reservoir, a gear pump, and a turbine flow meter. There are two separate loops in this system. The working fluid in the high-temperature loop will be Polyalphaolefin (PAO), while the fluid in the low-temperature loop will be pure ethylene glycol. Using pure ethylene glycol will avoid problems with bacterial growth. Proper parts have been identified for this system. Table 1.4 gives the specifications and costs of the major components.

A Solidworks model of this experiment has been developed including everything in the loop schematic and a model of the centrifuge table. As time progresses and parts are added to the experiment, the file can be updated to reflect the changes. Figure 1.15 shows the current design for the high-temperature fluid loop.

There are two major components that need to be fabricated. The cold plate consists of a ¼" thick copper plate with 3/8" OD copper tubing brazed to the surface. There are also holes that will be drilled into it for mounting to the table and affixing the heater to the cold plate. A model of the cold plate can be seen in Figure 1.16. The other fabricated item is the fill reservoir. This item will be made entirely of copper, with 4" ID copper tubing and two 3/16" copper plates soldered on top and bottom. There will be an inlet and outlet on the top for filling the reservoir, and another pair of ports located 180 degrees apart at the bottom of the reservoir for regular fluid flow. As can be seen from Figure 1.15, this reservoir is placed inboard of the pump to prevent the pump from being starved of PAO. The reservoir is necessary to help compensate for thermal expansion of the PAO when it gets heated. It also serves as a convenient location to fill the system of PAO. A model of the fill reservoir can be seen in Figure 1.17.

An 80/20 box will be placed around the cold plate portion of the high-temperature fluid loop. This box is to eliminate the forced convection created by the table while it is spinning. The outer edge the table can reach 25 MPH when the radial acceleration is

$a_r^+ = 9.0$. This will create a large amount of heat loss that will not be dumped into the cold plate. The cold plate is mounted vertically on the table to eliminate a large difference in acceleration between the inboard and outboard sides of the cold plate. When the loop heat pipe is mounted on the table, it will be mounted to the cold plate in a vertical fashion as well.

1.8 Progress to Date

Significant progress has been made toward developing an experiment to test the performance of a loop heat pipe under transient acceleration loading. The entire wiring system for the centrifuge has been analyzed and rebuilt. Wiring panels have been built to further facilitate the wiring of future experiments. A new data acquisition system has been implemented using LabVIEW to control it. The centrifuge table is controlled by specifying acceleration, not voltage. Work has begun on developing a high-temperature fluid loop for removing heat from the loop heat pipe. The recirculating chiller has been flushed and prepared for new ethylene glycol for use in the experiment. A Gantt chart showing tasks completed to date can be seen in Figure 1.18.

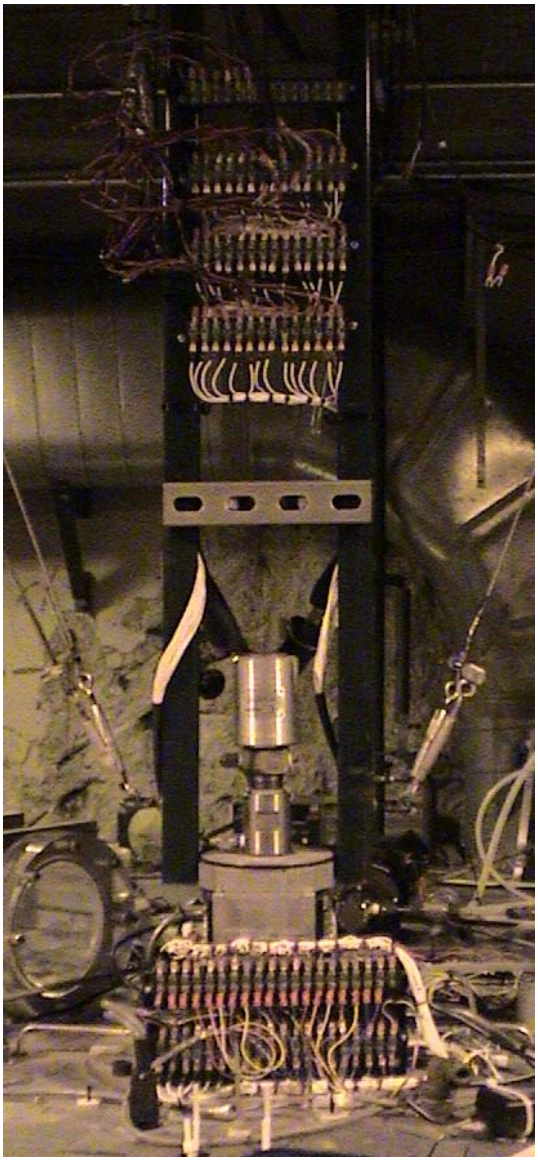

Figure 1.1. Updated wiring on the centrifuge table.

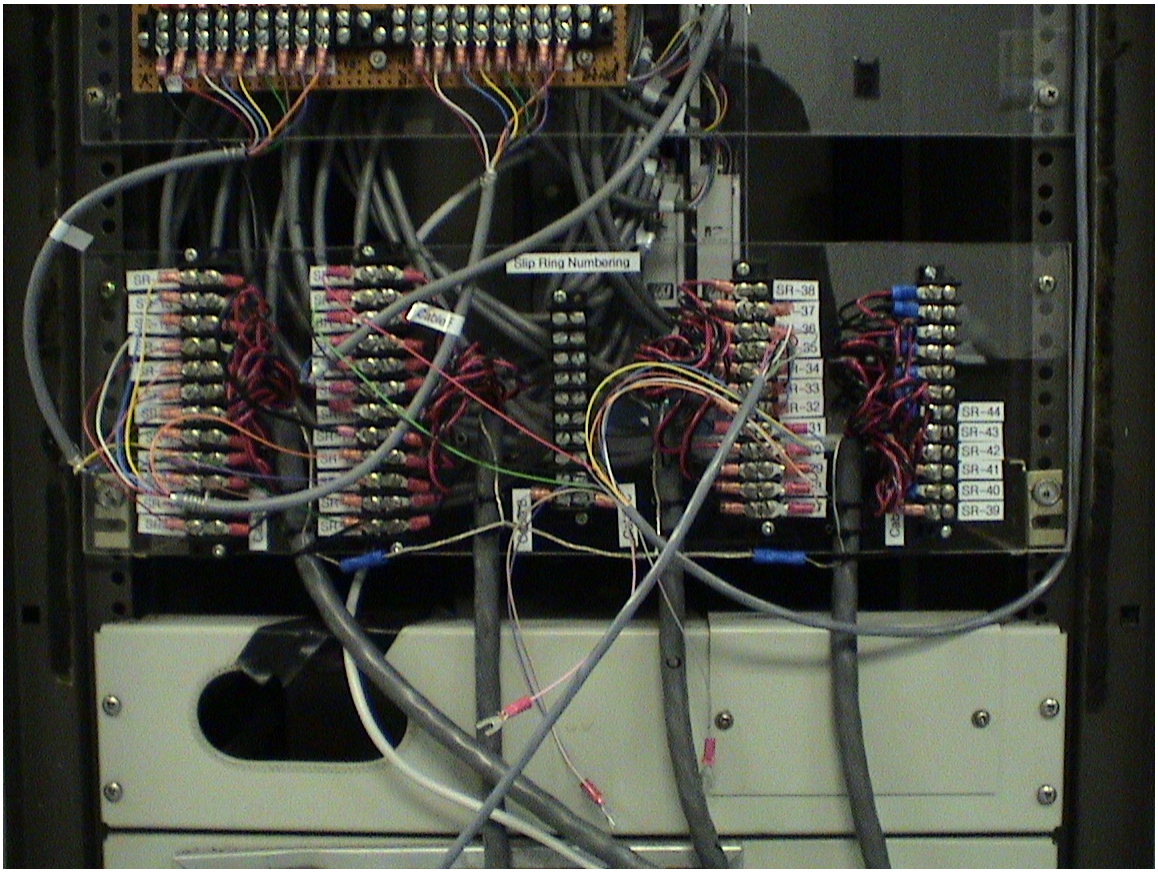

Figure 1.2. Wiring panel from centrifuge table to the centrifuge table control room.

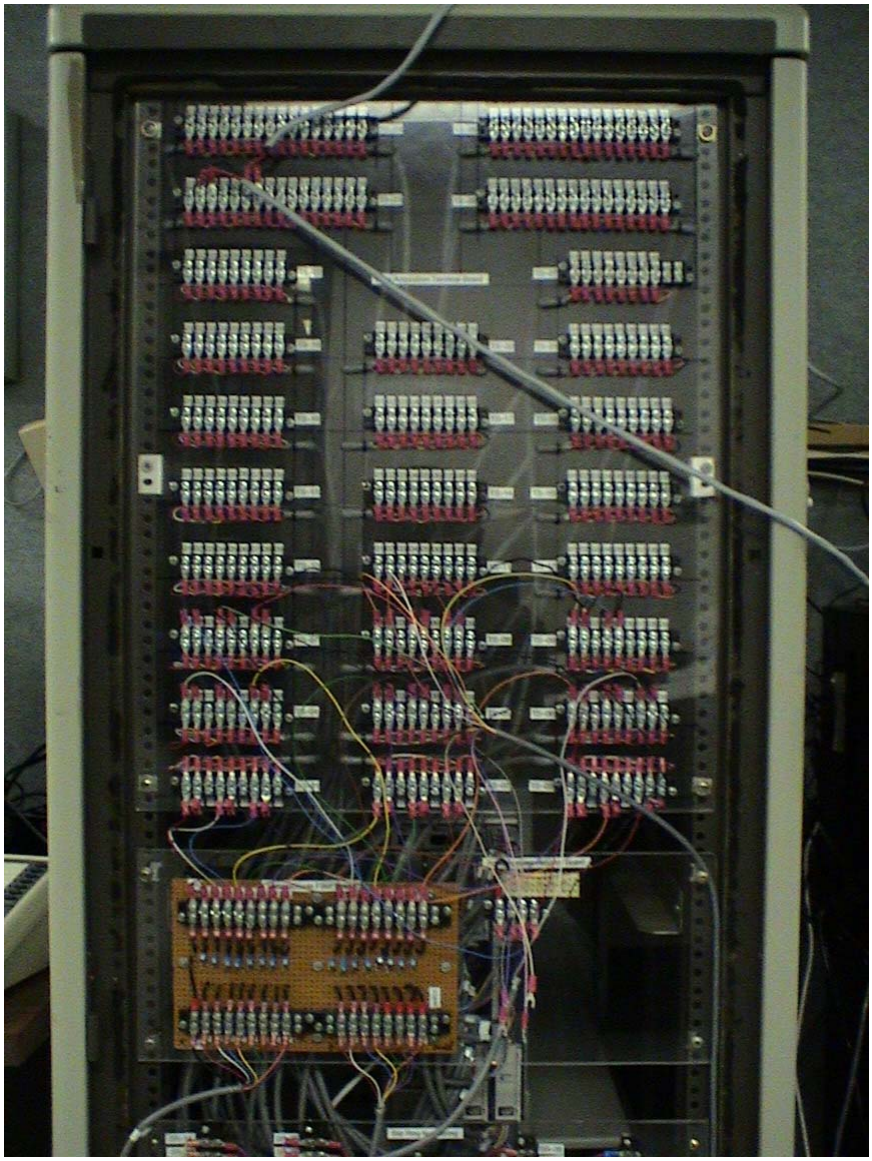

Figure 1.3. Wiring panel for the new data acquisition system.

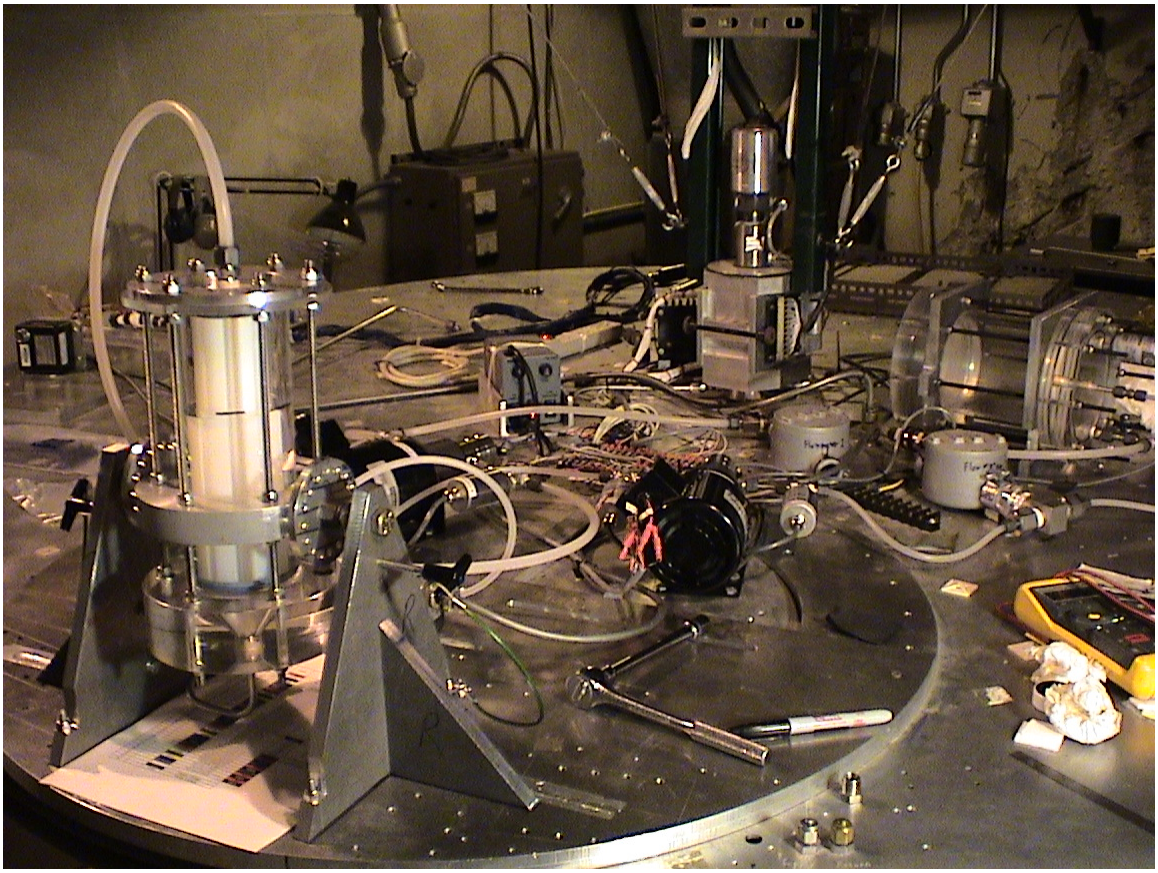

Figure 1.4. Liquid-vapor separator experiment controlled by custom LabVIEW VI.

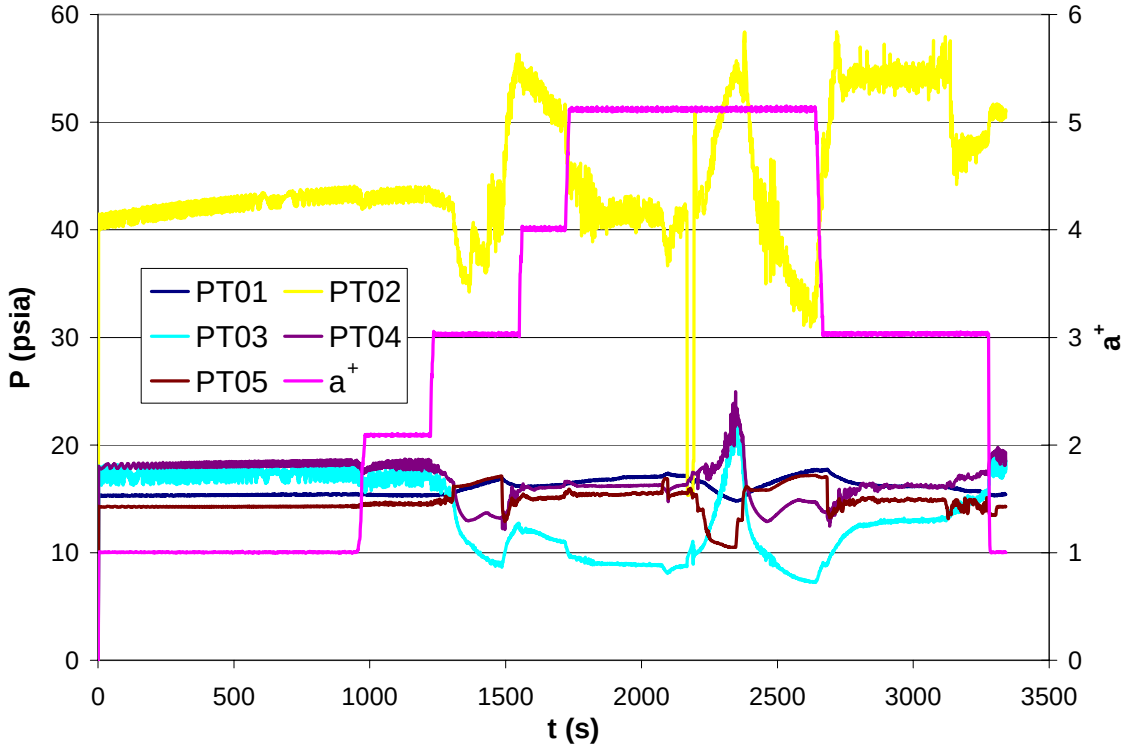

Figure 1.5. Sample raw data for the liquid-vapor separator experiment: Pressure and acceleration versus time.

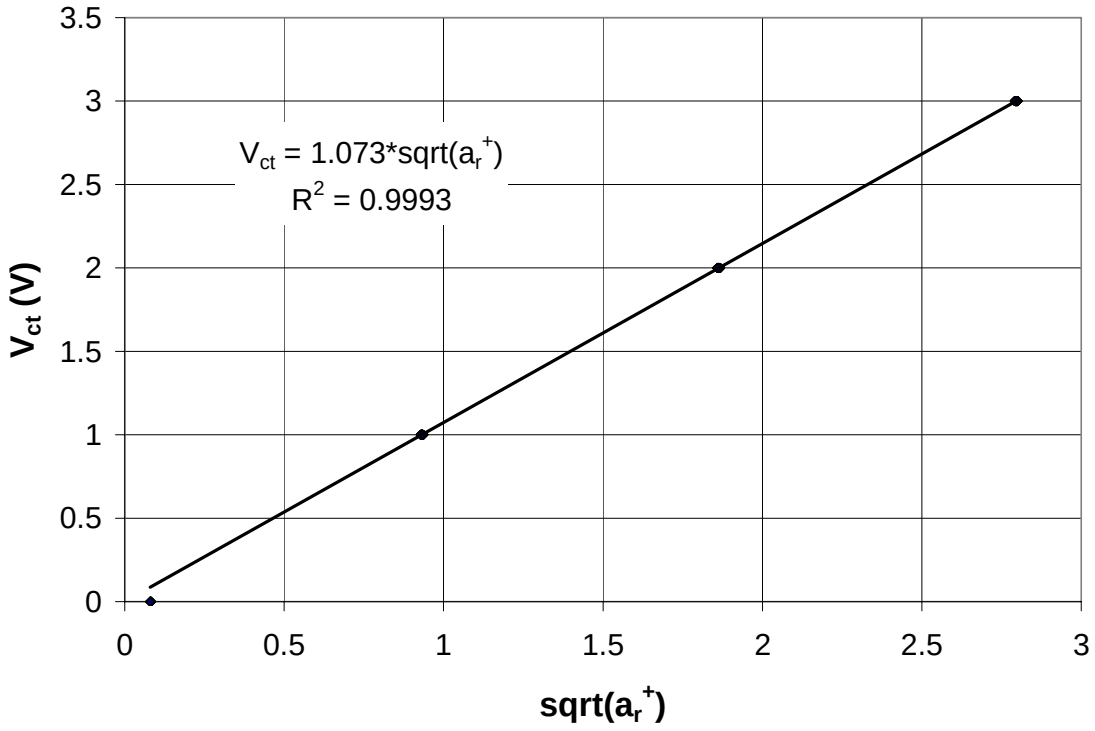

Figure 1.6. Centrifuge table voltage versus sqrt(a_r^+).

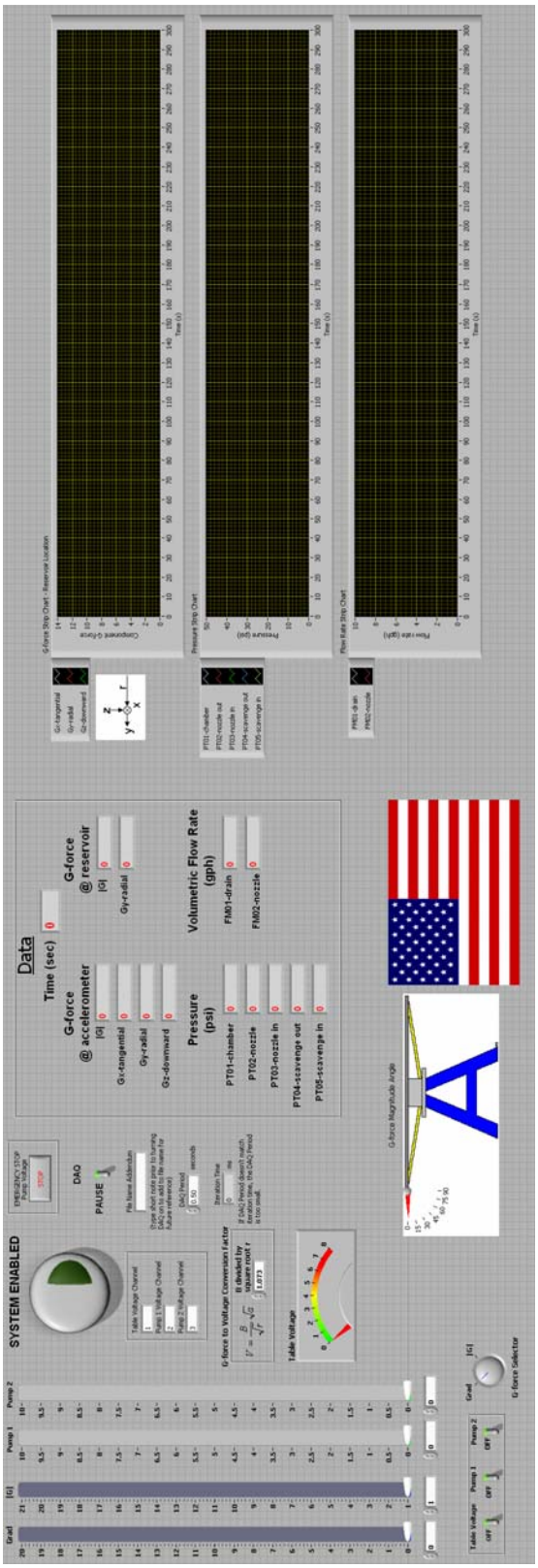

(a)

Figure 1.7. Example LabVIEW program: (a) Front panel; (b) Wiring diagram.

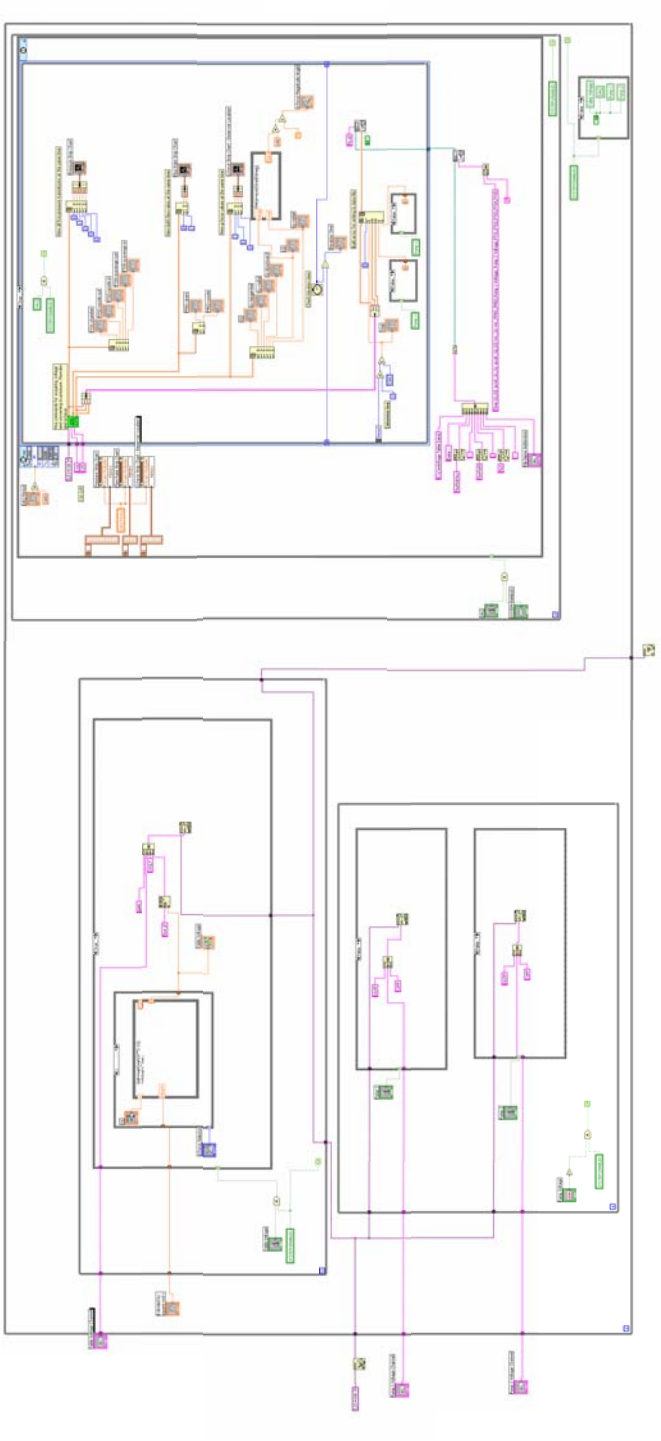

(b)

Figure 1.7, cont. Example LabVIEW program: (a) Front panel; (b) Wiring diagram.

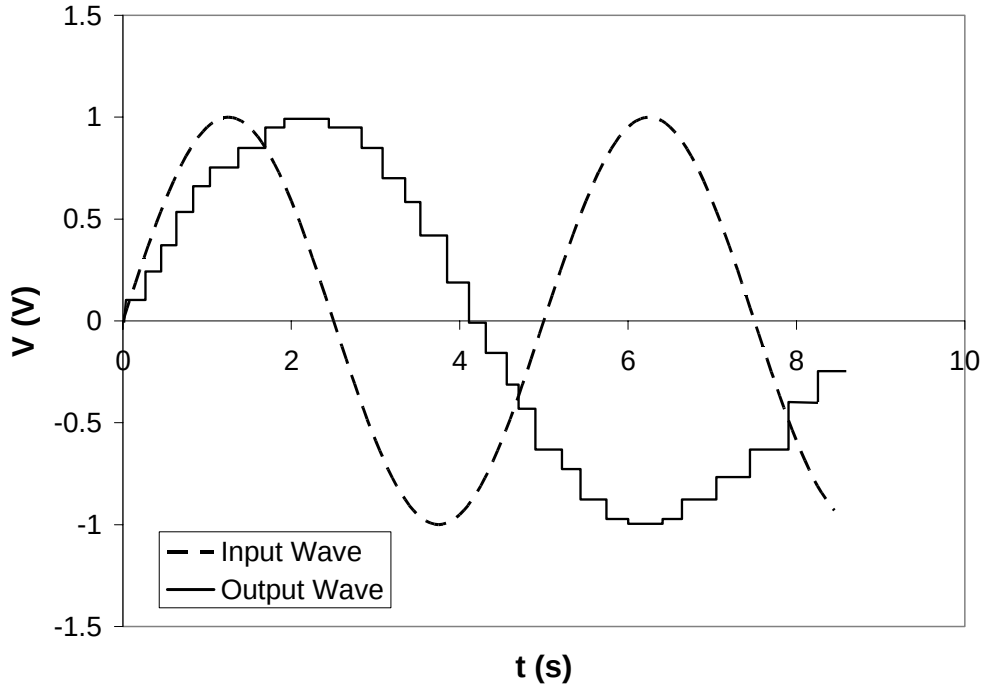

(a)

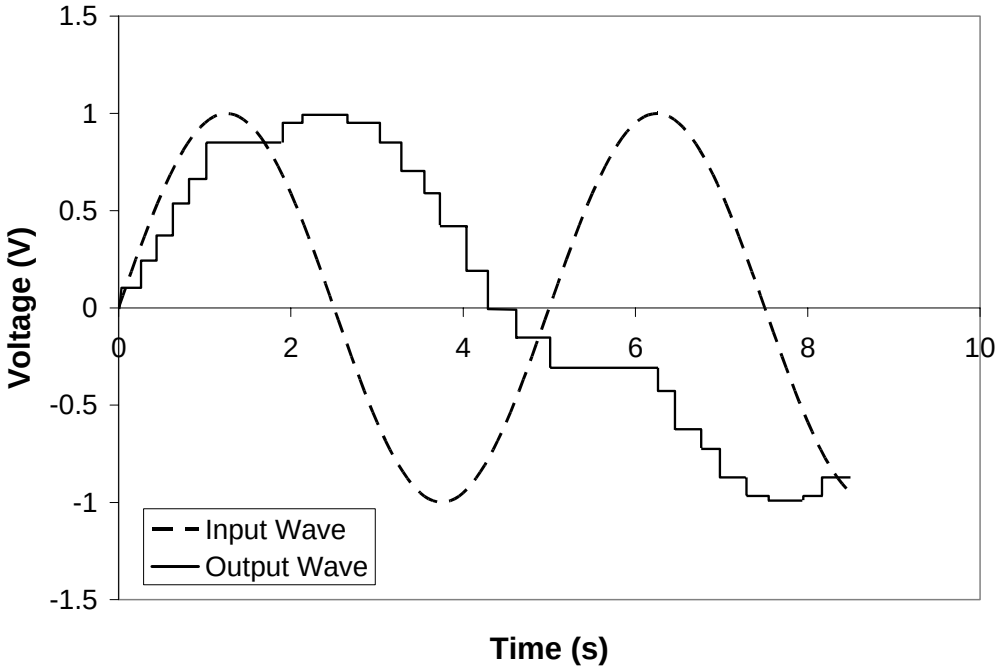

(b)

Figure 1.8. Simulated data of transient voltage control output: (a) Stair-stepped voltage output; (b) Pause in transient output due to data acquisition.

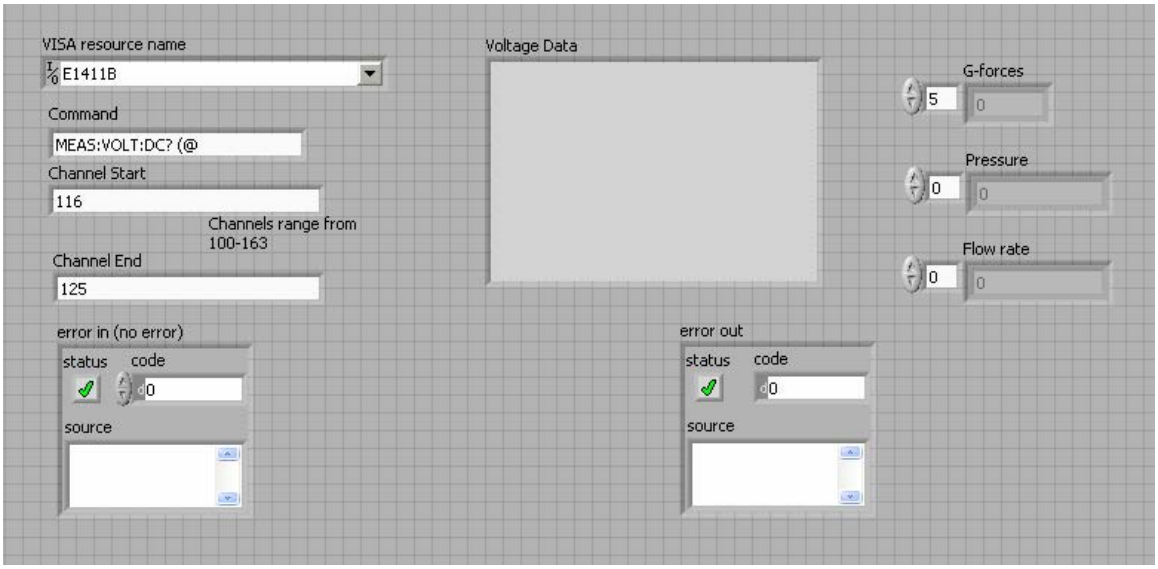

(a)

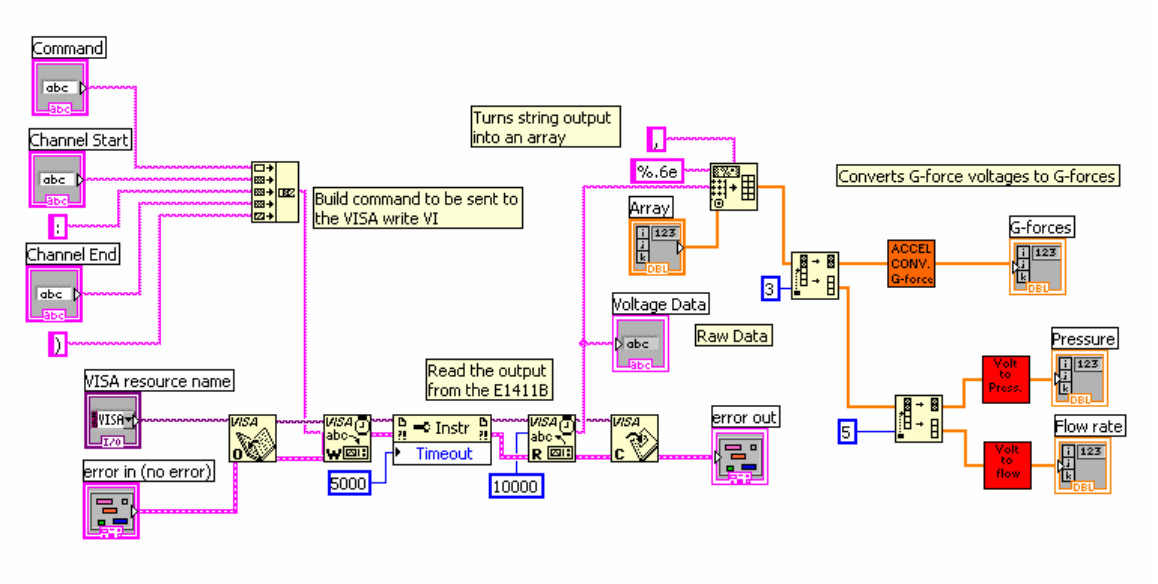

(b)

Figure 1.9. Text commands to read voltages and convert: (a) Front panel; (b) Wiring diagram.

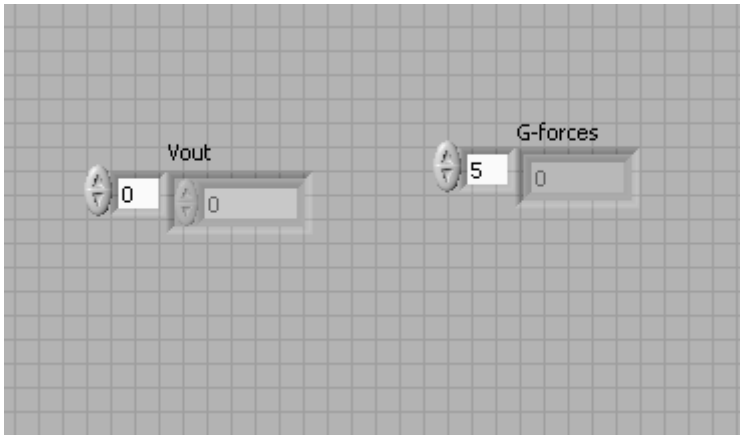

(a)

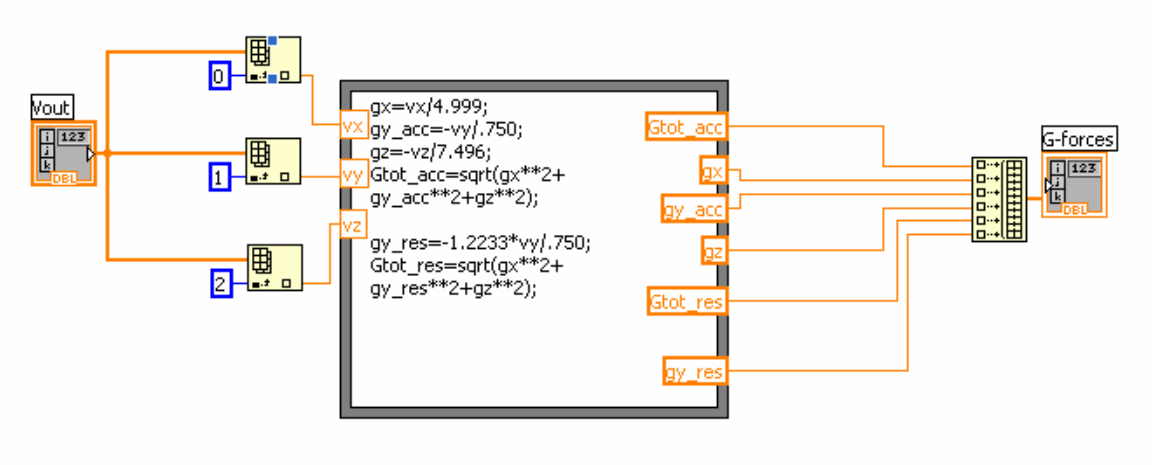

(b)

Figure 1.10. Voltage to acceleration conversion VI: (a) Front panel; (b) Wiring diagram.

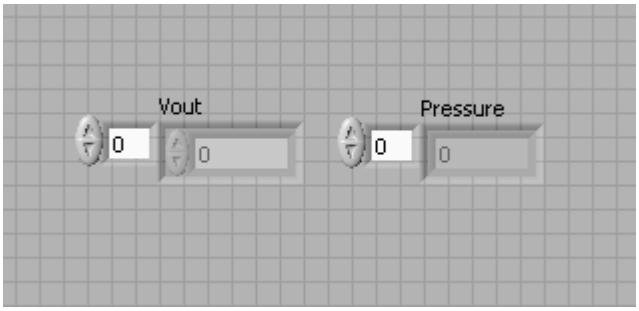

(a)

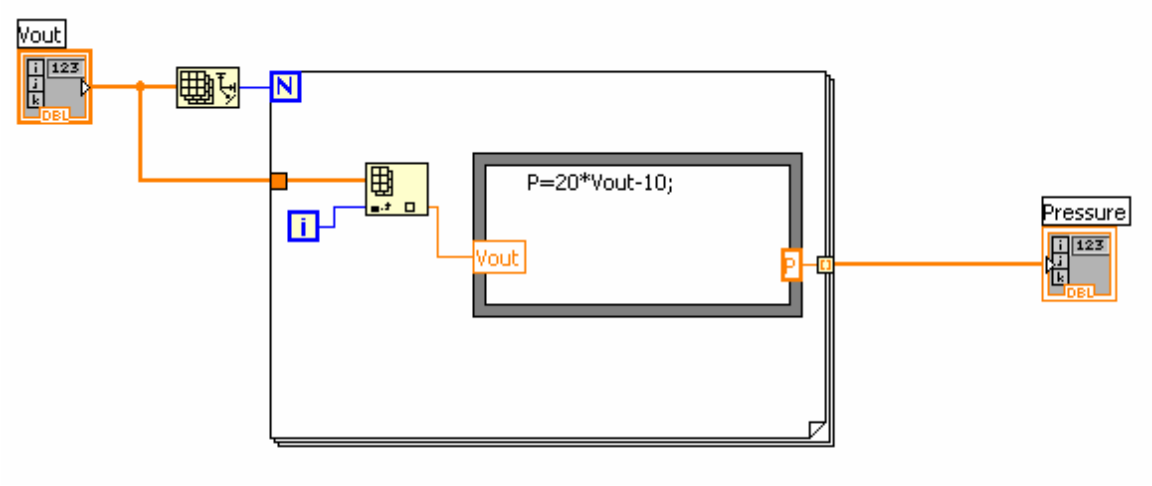

(b)

Figure 1.11. Voltage to pressure conversion VI: (a) Front panel; (b) Wiring diagram.

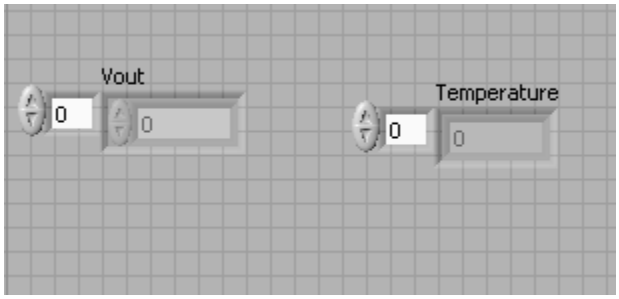

(a)

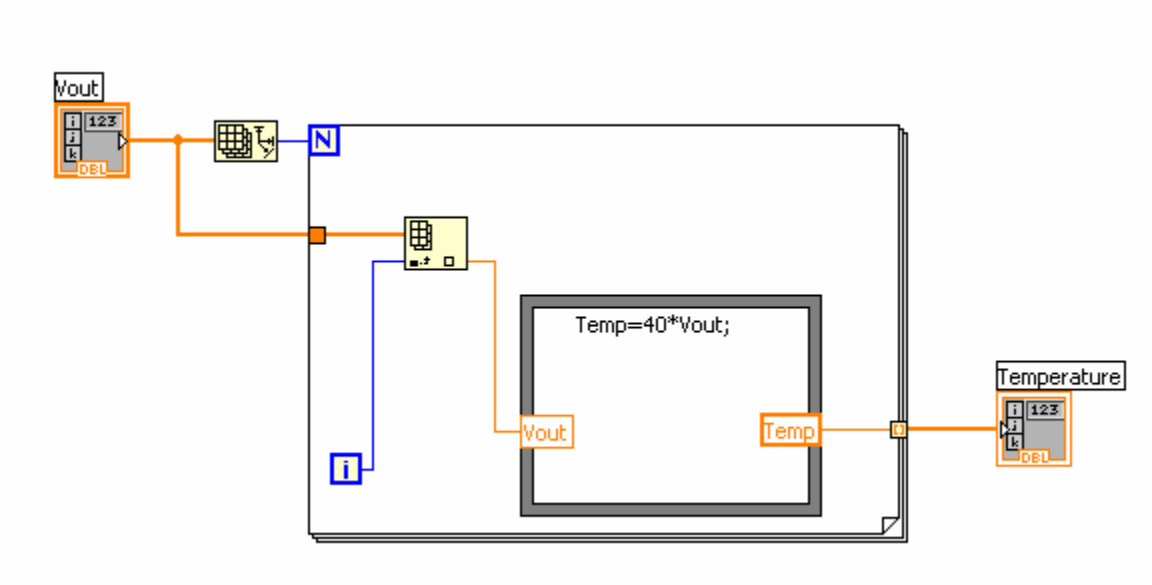

(b)

Figure 1.12. Voltage to temperature conversion VI: (a) Front panel; (b) Wiring diagram.

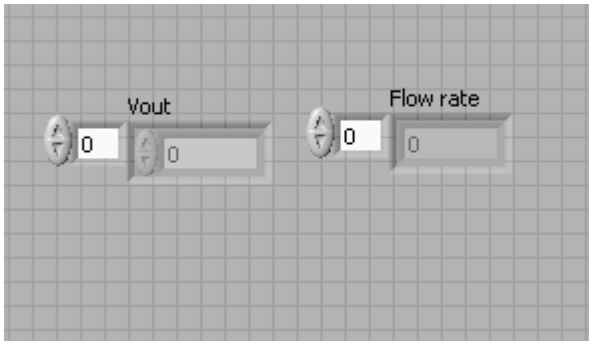

(a)

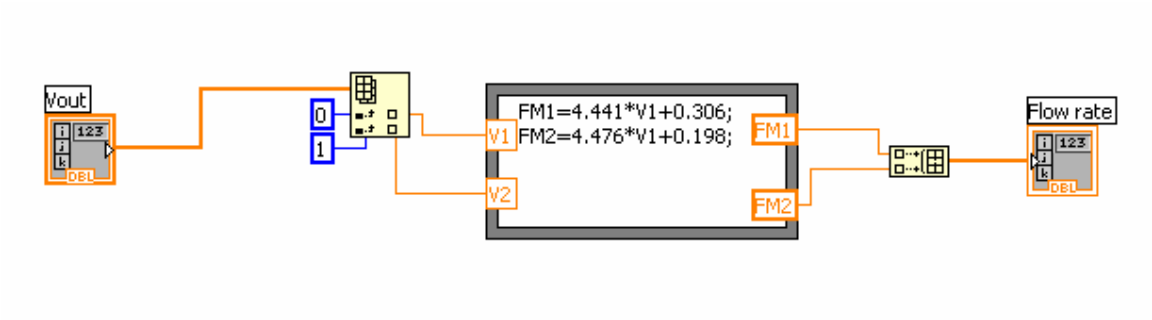

(b)

Figure 1.13. Voltage to volumetric flow rate conversion VI: (a) Front panel; (b) Wiring diagram.

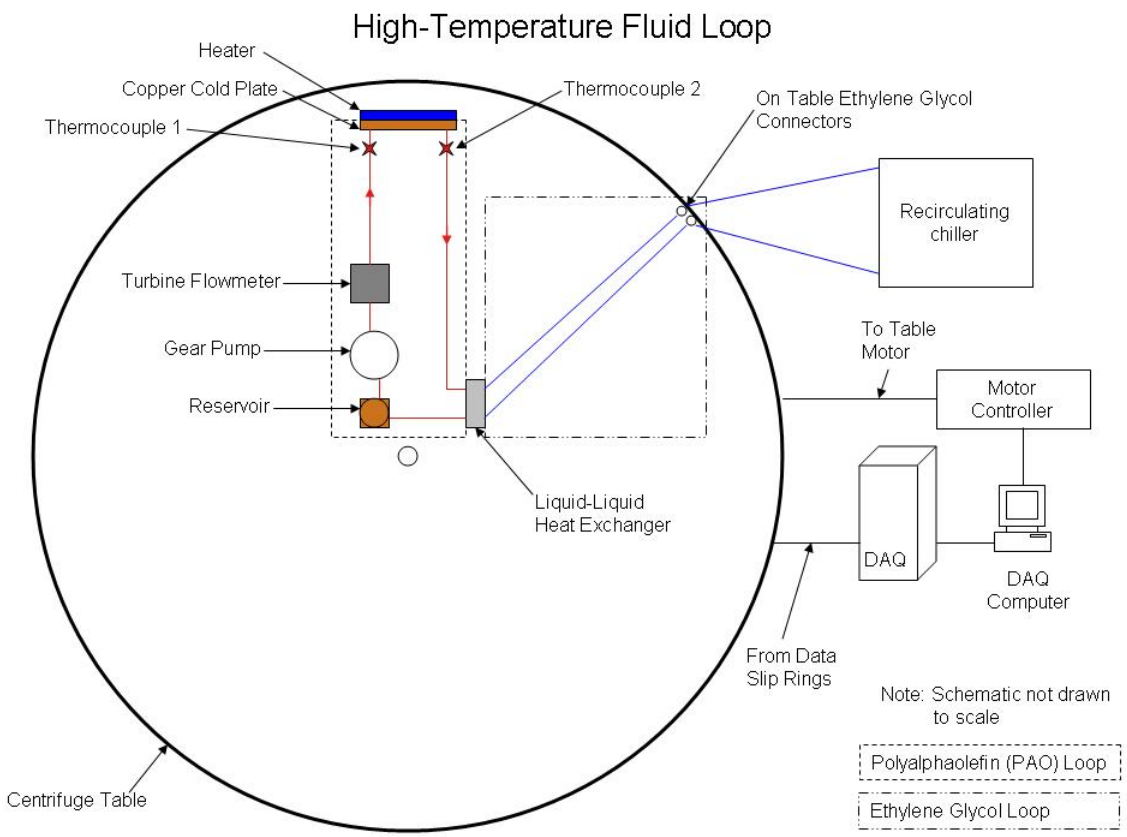

Figure 1.14. High-temperature fluid loop schematic.

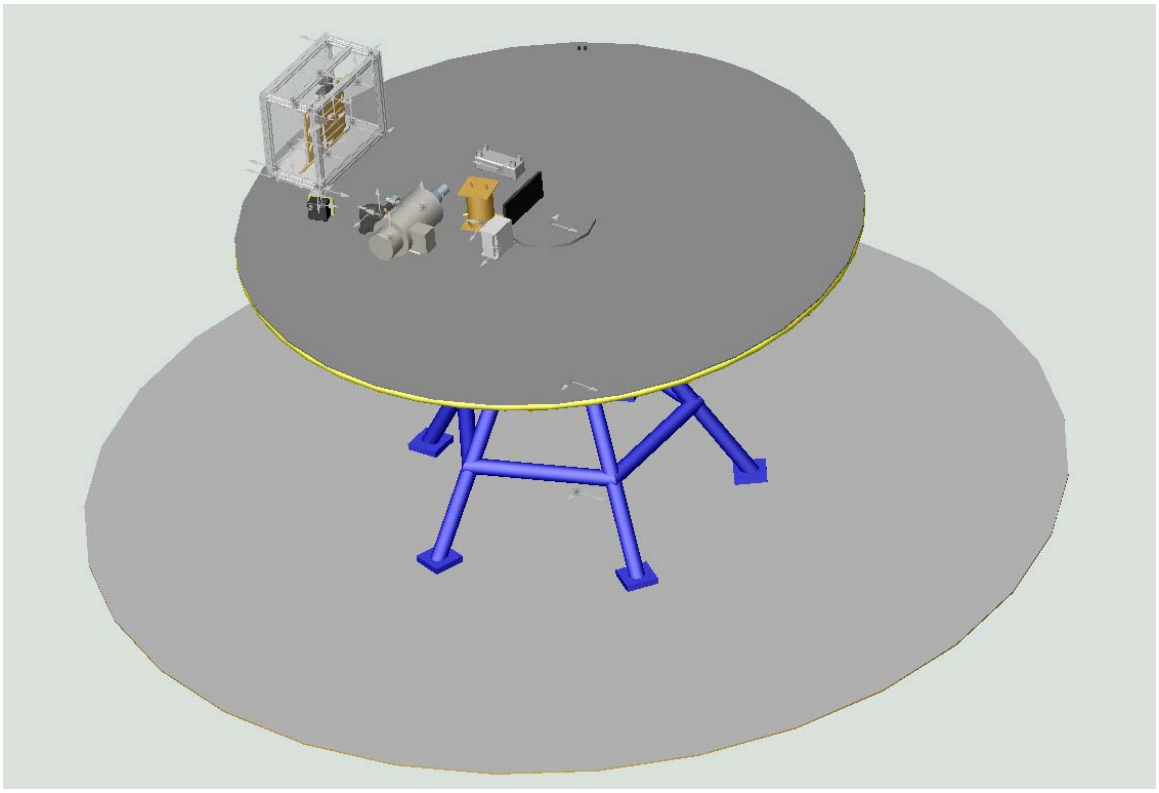

Figure 1.15. Solidworks model of high-temperature fluid loop.

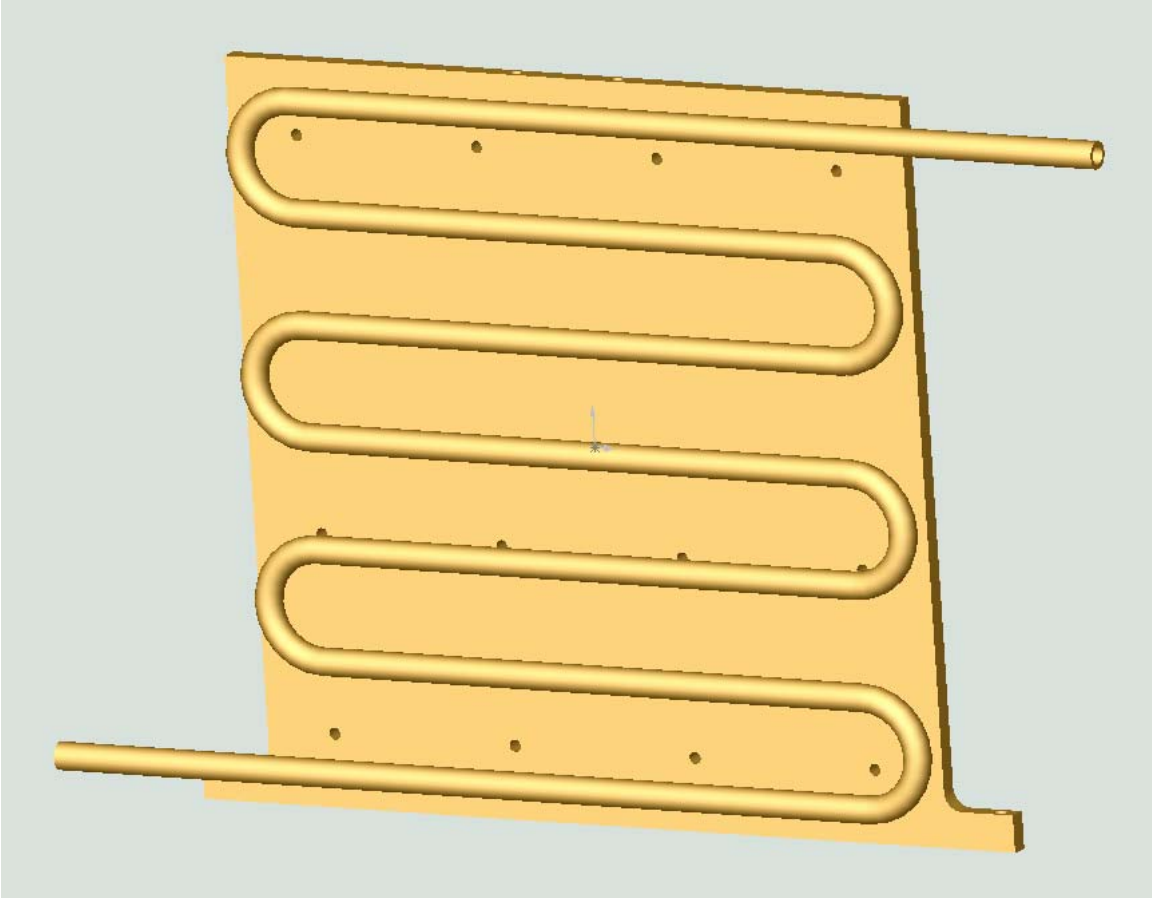

Figure 1.16. Model of copper cold plate.

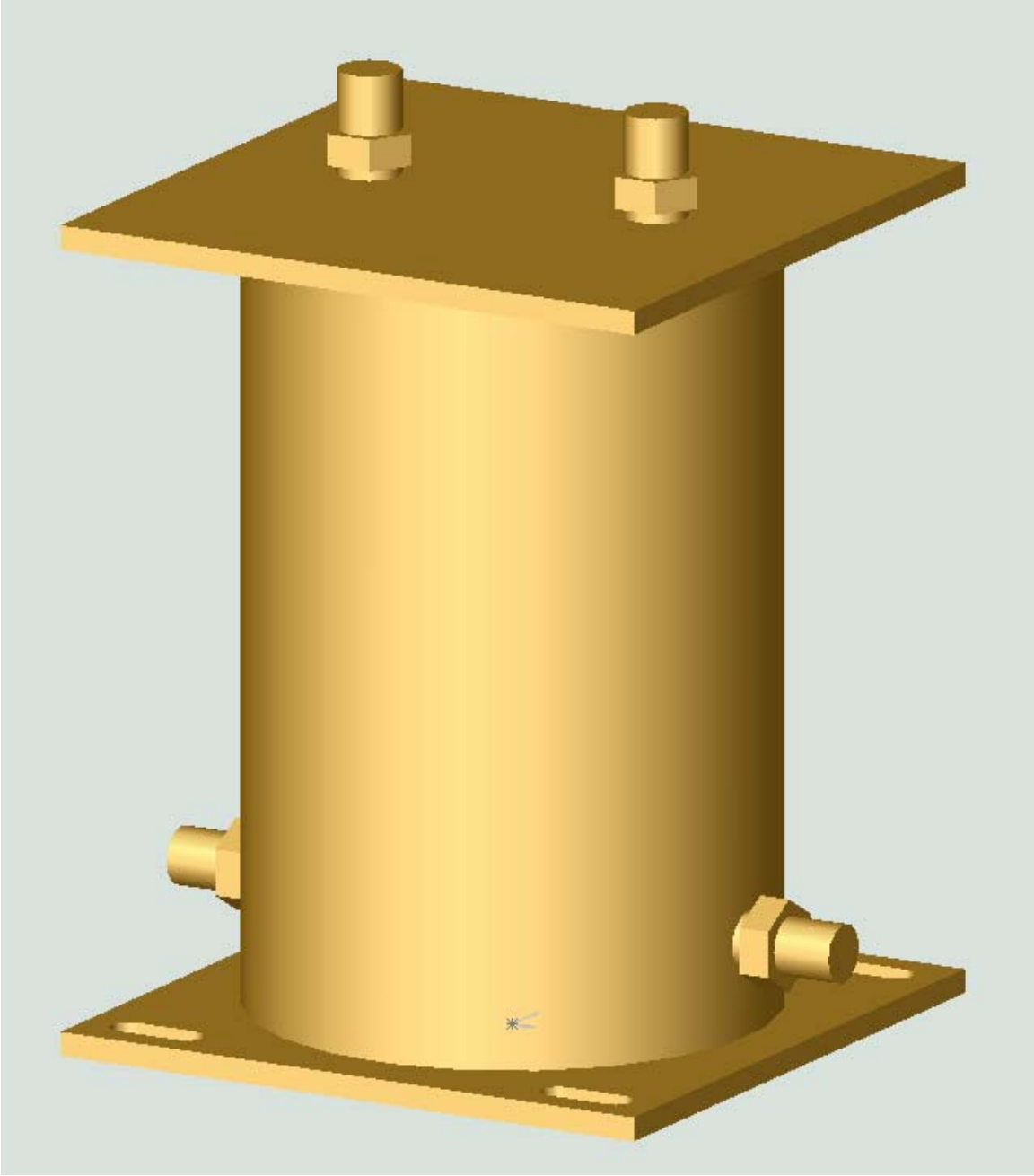

Figure 1.17. Model of fill reservoir.

Figure 1.18. Gantt chart of progress to date and projected schedule.

Table 1.1. Excel spreadsheet of wiring from the slip rings to the wiring panel.

Data Acquisition Terminal Board Wiring (Back of DataAcq Cabinet) (26Apr05)

E1476A Module Terminal Number	E1476A Terminal Letter	Main Terminal Strip Number	Main Terminal Number	Function	Slip Ring Number	Wire Color	TC Filter Board Terminal Number	Accel Board Terminal Number
00	H	01	01	TC01	3	red	01	
	L		02	TC Ground	19	black	GND	
	G		03					
01	H		04	TC02	4	white	02	
	L		05	TC Ground	19	black	GND	
	G		06					
02	H		07	TC03	5	blue	03	
	L		08	TC Ground	19	black	GND	
	G		09					
03	H	02	01	TC04	6	yellow	04	
	L		02	TC Ground	19	black	GND	
	G		03					
04	H		04	TC05	7	green	05	
	L		05	TC Ground	19	black	GND	
	G		06					
05	H		07	TC06	8	brown	06	
	L		08	TC Ground	19	black	GND	
	G		09					
06	H	03	01	TC07	9	purple	07	
	L		02	TC Ground	19	black	GND	
	G		03					
07	H		04	TC08	10	orange	08	
	L		05	TC Ground	19	black	GND	
	G		06					
08	H		07	TC09	11	red	09	
	L		08	TC Ground	19	black	GND	
	G		09					
09	H	04	01	TC10	12	white	10	
	L		02	TC Ground	19	black	GND	
	G		03					
10	H		04	TC11	13	blue	11	
	L		05	TC Ground	19	black	GND	
	G		06					
11	H		07	TC12	14	yellow	12	
	L		08	TC Ground	19	black	GND	
	G		09					
12	H	05	01	TC13	15	green	13	
	L		02	TC Ground	19	black	GND	
	G		03					
13	H		04	TC14	16	brown	14	
	L		05	TC Ground	19	black	GND	
	G		06					
14	H		07	TC15	17	purple	15	
	L		08	TC Ground	19	black	GND	
	G		09					

Table 1.1, cont. Excel spreadsheet of wiring from the slip rings to the wiring panel.

Data Acquisition Terminal Board Wiring (Back of DataAcq Cabinet) (26Apr05)

E1476A Module Terminal Number	E1476A Terminal Letter	Main Terminal Strip Number	Main Terminal Number	Function	Slip Ring Number	Wire Color	TC Filter Board Terminal Number	Accel Board Terminal Number
15	H	06	01	TC16	18	orange	16	
	L		02	TC Ground	19	black	GND	
	G		03					
16	H		04	Accel x-axis	21	red		2
	L		05	Accel GND	20	black		1
	G		06					
17	H		07	Accel y-axis	22	white		3
	L		08	Accel GND	20	black		1
	G		09					
18	H	07	01	Accel z-axis	23	blue		4
	L		02	Accel GND	20	black		1
	G		03					
19	H		04	PT01	25	green		
	L		05	PT/FM GND	24	black		
	G		06					
20	H		07	PT02	26	red		
	L		08	PT/FM GND	24	black		
	G		09					
21	H	08	01	PT03	27	orange		
	L		02	PT/FM GND	24	black		
	G		03					
22	H		04	PT04	28	white		
	L		05	PT/FM GND	24	black		
	G		06					
23	H		07	PT05	29	brown		
	L		08	PT/FM GND	24	black		
	G		09					
24	H	09	01	FM01	30	yellow		
	L		02	PT/FM GND	24	black		
	G		03					
25	H		04	FM02	31	blue		
	L		05	PT/FM GND	24	black		
	G		06					
26	H		07					
	L		08					
	G		09					
27	H	10	01					
	L		02					
	G		03					
28	H		04					
	L		05					
	G		06					
29	H		07					
	L		08					
	G		09					

Table 1.1, cont. Excel spreadsheet of wiring from the slip rings to the wiring panel.

Data Acquisition Terminal Board Wiring (Back of DataAcq Cabinet) (26Apr05)

E1476A Module Terminal Number	E1476A Terminal Letter	Main Terminal Strip Number	Main Terminal Number	Function	Slip Ring Number	Wire Color	TC Filter Board Terminal Number	Accel Board Terminal Number
30	H	11	01					
	L		02					
	G		03					
31	H		04					
	L		05					
	G		06					
32	H		07					
	L		08					
	G		09					
33	H	12	01					
	L		02					
	G		03					
34	H		04					
	L		05					
	G		06					
35	H		07					
	L		08					
	G		09					
36	H	13	01					
	L		02					
	G		03					
37	H		04					
	L		05					
	G		06					
38	H		07					
	L		08					
	G		09					
39	H	14	01					
	L		02					
	G		03					
40	H		04					
	L		05					
	G		06					
41	H		07					
	L		08					
	G		09					
42	H	15	01					
	L		02					
	G		03					
43	H		04					
	L		05					
	G		06					
44	H		07					
	L		08					
	G		09					

Table 1.1, cont. Excel spreadsheet of wiring from the slip rings to the wiring panel.

Data Acquisition Terminal Board Wiring (Back of DataAcq Cabinet) (26Apr05)

E1476A Module Terminal Number	E1476A Terminal Letter	Main Terminal Strip Number	Main Terminal Number	Function	Slip Ring Number	Wire Color	TC Filter Board Terminal Number	Accel Board Terminal Number
45	H	16	01					
	L		02					
	G		03					
46	H		04					
	L		05					
	G		06					
47	H		07					
	L		08					
	G		09					
48	H	17	01					
	L		02					
	G		03					
49	H		04					
	L		05					
	G		06					
50	H		07					
	L		08					
	G		09					
51	H	18	01					
	L		02					
	G		03					
52	H		04					
	L		05					
	G		06					
53	H		07					
	L		08					
	G		09					
54	H	19	01					
	L		02					
	G		03					
55	H		04					
	L		05					
	G		06					
56	H		07					
	L		08					
	G		09					
57	H	20	01					
	L		02					
	G		03					
58	H		04					
	L		05					
	G		06					
59	H		07					
	L		08					
	G		09					

Table 1.1, cont. Excel spreadsheet of wiring from the slip rings to the wiring panel.

Data Acquisition Terminal Board Wiring (Back of DataAcq Cabinet) (26Apr05)

E1476A Module Terminal Number	E1476A Terminal Letter	Main Terminal Strip Number	Main Terminal Number	Function	Slip Ring Number	Wire Color	TC Filter Board Terminal Number	Accel Board Terminal Number
60	H	21	01					
	L		02					
	G		03					
61	H		04					
	L		05					
	G		06					
62	H		07					
	L		08					
	G		09					
63	H	22	01					
	L		02					
	G		03					
VM Input	H		04					
	L		05					
	G		06					
VM Ω I	H		07					
	L		08					
	G		09					

Table 1.2. Excel spreadsheet of wiring for the D/A converter.

E1418A 8/16-CH D/A Converter Wiring (08Dec04)

Module Terminal Number	Terminal Letter	Wire Bundle Number	Wire Color	Terminal Strip Number	Terminal Number
1	HS	23	red	23	01
	HI		white		02
	LO		blue		03
	LS		yellow		04
2	HS		green		05
	HI		brown		06
	LO		purple		07
	LS		orange		08
3	HS	24	red		09
	HI		white		10
	LO		blue		11
	LS		yellow		12
4	HS		green		13
	HI		brown		14
	LO		purple		15
	LS		orange		16
5	HS	25	red	24	01
	HI		white		02
	LO		blue		03
	LS		yellow		04
6	HS		green		05
	HI		brown		06
	LO		purple		07
	LS		orange		08
7	HS	26	red		09
	HI		white		10
	LO		blue		11
	LS		yellow		12
8	HS		green		13
	HI		brown		14
	LO		purple		15
	LS		orange		16

Table 1.2, cont'd. Excel spreadsheet of wiring for the D/A converter.

E1418A 8/16-CH D/A Converter Wiring (08Dec04)

Module Terminal Number	Terminal Letter	Wire Bundle Number	Wire Color	Terminal Strip Number	Terminal Number
9	HS	27	red	25	01
	HI		white		02
	LO		blue		03
	LS		yellow		04
10	HS		green		05
	HI		brown		06
	LO		purple		07
	LS		orange		08
11	HS	28	red		09
	HI		white		10
	LO		blue		11
	LS		yellow		12
12	HS		green		13
	HI		brown		14
	LO		purple		15
	LS		orange		16
13	HS	29	red	26	01
	HI		white		02
	LO		blue		03
	LS		yellow		04
14	HS		green		05
	HI		brown		06
	LO		purple		07
	LS		orange		08
15	HS	30	red		09
	HI		white		10
	LO		blue		11
	LS		yellow		12
16	HS		green		13
	HI		brown		14
	LO		purple		15
	LS		orange		16
	GND	31	red	27	01
	EXT TRIGn		white		02
	GND		blue		03
	GND		yellow		04
	CAL HS		green		05
	CAL HI		brown		06
	CAL LO		purple		07
	CAL LS		orange		08

Table 1.3. Recirculating chiller flow rates: (a) Without booster pump; (b) With booster pump.

Without Booster Pump			
Trial	Time (s)	Volume (L)	Volumetric Flow Rate (LPM)
1	137	2.0	0.876
2	136	2.0	0.882
3	137	2.0	0.876

(a)

With Booster Pump				
Trial	Pump Setting	Times (s)	Volume (L)	Volumetric Flow Rate (LPM)
1	30	71	2.0	1.690
2	40	63	2.0	1.905
3	50	54	2.0	2.222

(b)

Table 1.4. Proposed costs of major components for high-temperature fluid loop.

Major Required Parts	Company	Vendor	Model No.	Item Cost	Qty.	Total Cost
Heater	Minco	Minco	HM6829R23.2L12T1U	$85.80	1	$85.80
Liquid-Liquid Heat Exchanger	Lytron	In-house	LL520	$0.00	1	$0.00
Pumphead, Motor, Controller	Tuthill	Premier	DXS.68EEET2WNF10G9	$2,155.00	1	$2,155.00
Turbine Flowmeter	Omega	Omega	FTB9504	$727.00	1	$727.00
Signal Conditioner	Omega	Omega	FLSC-61	$325.00	1	$325.00
Thermocouple Type T (Exposed Tip)	Omega	Omega	TMQSS-062E-6	$24.00	2	$48.00
Copper Plate 10" x 10"	McMaster	McMaster	89675K37	$141.86	1	$141.86
Copper Tube 4 1/8" OD x 12"	Pickrel Bros	Pickrel Bros.	-	$38.64	1	$38.64
Copper Plate 12" x 12"	McMaster	McMaster	8995K12	$117.02	1	$117.02
				Total		$3,638.32

Chapter 2: Mathematical Model of Aerodynamic Heating for High-Speed Aircraft

2.1 Introduction

The More-Electric Aircraft initiative (MEA) has resulted in the development of high-temperature, high-efficiency, and high-density power electronic component technologies. The next-generation power electronics will operate at cold plate temperatures of up to 200ºC, which presents an opportunity to reject heat through the aircraft skin to the ambient using passive cooling. Possible thermal management scenarios include a direct connection of the electronics package to the skin or the use of a loop heat pipe between the package and the skin to provide mounting flexibility.

The operating envelope for military aircraft places stringent requirements on any proposed thermal management system. The on-board electrical flight control actuation system operates at altitudes from sea level to above 40 kft, airspeeds from stationary to supersonic speeds, transient body forces up to 9-g due to maneuvering, and ambient temperatures from -80 to 45ºC. In addition, the actuation system rejects heat continuously at a rate of 500 W (~3 W/cm^2) and has transient heat rejection rates of 5000 W over a period of one second. Therefore, the above-mentioned thermal management scenarios may have to be augmented by the use of a solid-liquid phase change thermal energy storage approach. Phase change materials (PCMs) have very large capacities to absorb and reject heat at nearly constant temperatures without significant volumetric changes. The use of a PCM thermal energy storage media could average out the high heat flux transient heat loads and allow a more compact and lightweight thermal management system. While PCMs typically have low thermal conductivities, recent efforts using a high thermal conductivity foam filled with PCM has distinct possibilities to improve the viability of the use of PCMs.

The objective of the present analysis is to determine the feasibility of using loop heat pipes to dissipate waste heat from power electronics to the skin of a fighter aircraft. In the past, it has been found that the boundary condition at the condenser can be a controlling factor in the overall performance of this type of thermal management scheme. Therefore, the heat transfer removed from the aircraft skin has been determined as a

function of Mach number, altitude, and skin temperature by modeling the wing as a flat plate at zero-incidence. In addition, the effects of the variable properties of air have been taken into account. Heat transfer due to thermal radiation has been neglected in this analysis due to the low skin temperatures and high airspeeds.

2.2 Mathematical Model

The temperature and density of air vary considerably with altitude and also vary day-to-day depending on weather conditions. In order to be conservative in the calculation of heat transfer coefficients, data for the highest temperature recorded with a frequency-of-occurrence of 1% were used to generate equations for temperature and density versus altitude (DOD, 1997) as shown in Figure 2.1 and Figure 2.2 and Table 2.1. Also presented are data for the lowest temperature recorded with a frequency-of-occurrence of 1% (DOD, 1997) and data for the "standard atmosphere" (Anderson, 2000).

The film temperature was used to evaluate the air properties (White, 1988)

$$T^* = T_\infty(0.5 + 0.039\mathrm{Ma}_\infty^2) + 0.5T_w \tag{2.1}$$

The air density at the film temperature and at altitude was evaluated using the perfect gas law

$$\rho^* = \rho_\infty\left(\frac{T_\infty}{T^*}\right) \tag{2.2}$$

The freestream speed of sound is

$$a_\infty = \sqrt{\gamma R T_\infty} \tag{2.3}$$

The freestream velocity is

$$U_\infty = \mathrm{Ma}_\infty a_\infty \tag{2.4}$$

The absolute viscosity of air is given by the following relation (NACA, 1953)

$$\mu = \mu_{\mathrm{R}} \left(\frac{T}{T_{\mathrm{R}}} \right)^{0.76} \tag{2.5}$$

where μ_{R} is a reference viscosity evaluated at some reference temperature T_{R}.

The Reynolds number for a plate of length L is determined by evaluating the properties of air at the freestream condition.

$$\mathrm{Re}_{\mathrm{L}} = \frac{\rho_{\infty} U_{\infty} L}{\mu_{\infty}} \tag{2.6}$$

Regression equations for the specific heat and Prandtl number were determined as functions of temperature using data from Incropera and DeWitt (1990), as shown in Figure 2.3 and Figure 2.4 and Table 2.2.

The adiabatic wall temperature is (White, 1988)

$$T_{\mathrm{aw}} = T_{\infty} \left[1 + r \left(\frac{\gamma - 1}{2} \right) \mathrm{Ma}_{\infty}^{2} \right] \tag{2.7}$$

where the recovery factor is

$$r = \begin{cases} \mathrm{Pr}^{1/2} & \text{for laminar flow} \\ \mathrm{Pr}^{1/3} & \text{for turbulent flow} \end{cases} \tag{2.8}$$

The local skin friction coefficient at the end of the plate is found by evaluating the air properties at the film temperature (White, 1988).

$$C_{\mathrm{f,L}}^{*} = \frac{0.455}{\ln^{2}\left(0.06\rho^{*}U_{\infty}L/\mu^{*}\right)} \tag{2.9}$$

The local Stanton number at the end of the plate is given by (White, 1988)

$$\mathrm{St}_{\mathrm{L}}^{*} = \frac{h_{\mathrm{L}}}{\rho^{*}U_{\infty}c_{\mathrm{p}}^{*}} = \frac{C_{\mathrm{f,L}}^{*}/2}{1+12.7(\mathrm{Pr}^{*2/3}-1)(C_{\mathrm{f,L}}^{*}/2)^{1/2}} \tag{2.10}$$

The local heat transfer coefficient at the end of the plate is

$$h_{\mathrm{L}} = \mathrm{St}_{\mathrm{L}}^{*}\rho^{*}U_{\infty}c_{\mathrm{p}}^{*} \tag{2.11}$$

The average heat transfer coefficient over the length of the plate is approximated by (White, 1988)

$$\bar{h} = 1.15h_{\mathrm{L}} \tag{2.12}$$

The average heat flux dissipated over the plate is defined in terms of the adiabatic wall temperature (White, 1988)

$$q_{\mathrm{w}}^{''} = \bar{h}(T_{\mathrm{s}} - T_{\mathrm{aw}}) \tag{2.13}$$

Now that the external boundary condition on the skin has been described, a model of the heat conduction from the electronics package through the skin will be developed. Two scenarios will be examined: Direct mounting of the electronics package to the skin, and mounting a loop heat pipe between the electronics package and the aircraft skin. It is

assumed that the conduction of heat through the system is one-dimensional, the thermal properties are constant, and that the system is under steady state conditions.

2.2.1 Scenario 1: Direct mounting to the skin

The electronics package is directly mounted to the aircraft skin as shown in Figure 2.5(a). A heat spreader has been included between the package and the skin to provide for the possibility of reducing the heat flux to the skin. An agent to reduce contact resistance, such as thermal grease, is present between the faces of the package, the thermal spreader, and the interior aircraft skin. The maximum temperatures of the electronics package and the aircraft skin and the heat dissipation rate from the package are known. The objective of this part of the analysis is to determine the external conditions for which the maximum skin temperature and/or the maximum temperature of the package are reached. An equivalent thermal circuit of the one-dimensional heat conduction problem is shown in Figure 2.5(b). The contact resistances are given by R1 and R3. The thermal resistance within the heat spreader is R2, and that of the aircraft skin is R4. The convective thermal resistance from the skin to the freestream is R5. Based on the analysis of the turbulent flow over a flat plate, the outer skin temperature is found by solving the following equation.

$$\bar{h}L_3^2(T_5 - T_{\text{aw}}) - q_{\text{x}} = 0 \tag{2.14}$$

Eq. (2.14) must be solved iteratively due to the dependence of the convective heat transfer coefficient on the wall temperature through the dependence of the air properties on the film temperature, as outlined in Eq. **(2.1)**. The inner skin temperature is found using Fourier's law.

$$T_4 = T_5 + \frac{q_{\text{x}} t_{\text{s}}}{k_{\text{s}} L_3^2} \tag{2.15}$$

The temperature on the right-hand face of the heat spreader is determined by taking the contact resistance into account.

$$T_3 = T_4 + \frac{q_x R_c''}{L_3^2} \tag{2.16}$$

The temperature distribution through the heat spreader can be found by assuming that it is a truncated pyramid with a square cross section. The cross-sectional area of the truncated pyramid is

$$A(x) = ax^2 + b = \left(\frac{L_3^2 - L_2^2}{t_{hs}^2} \right) x^2 + L_2^2 \tag{2.17}$$

Fourier's law can then be used to determine the temperature distribution by separating variables and integrating

$$q_x = -k_{hs} A \frac{dT}{dx} = -k_{hs} \left(ax^2 + b \right) \frac{dT}{dx} \tag{2.18}$$

$$-\frac{q_x}{k_{hs}} \int_0^x \frac{d\eta}{\left(a\eta^2 + b \right)} = \int_{T_2}^{T} d\tau \tag{2.19}$$

where η and τ are dummy variables. The temperature distribution through the heat spreader is given by

$$T - T_2 = -\frac{q_x}{k_{hs}\sqrt{ab}} \cdot \tan^{-1}\left(\frac{x\sqrt{ab}}{b} \right) \tag{2.20}$$

The temperature at the left-hand face of the heat spreader is

$$T_2 = T_3 + \frac{q_x}{k_{hs}\sqrt{ab}} \cdot \tan^{-1}\left(\frac{t_{hs}\sqrt{ab}}{b} \right) \tag{2.21}$$

The temperature of the face of the electronics package at point 1 is

$$T_1 = T_2 + \frac{q_x R_c^{"}}{L_2^2} \tag{2.22}$$

2.3 Results and Discussion

The analysis for high-speed flow of air over a flat plate at altitude was validated using the results of Leland et al. (2004) as shown in Table 2.3. Three separate cases were compared using the 1% hot day data in which the altitude was H = 0, 5000, and 40,000 ft and the Mach number was Ma_∞ = 0.98 and 1.4. For all cases, the plate length was L = 1.0 m and the temperature of the plate was T_w = 135 °C. The results of the comparison are excellent with a maximum difference for the average heat transfer coefficient of less than 2%.

The adiabatic wall temperature is shown in Figure 2.6 as a function of altitude and Mach number. The overall trend of the adiabatic wall temperature with altitude follows the freestream air temperature in Figure 2.1 and increases with Mach number as expected. Figure 2.7 presents the temperature difference, $\Delta T = (T_{aw}\text{-}T_\infty)$, versus altitude. This temperature difference demonstrates the increase in the adiabatic wall temperature over the freestream due to aerodynamic heating. The temperature difference $\Delta T = (T_w\text{-}T_{aw})$, a defining factor in heat flux, is given in Figure 2.8. Of interest is the portion of the curves in which this difference is negative, which indicates that heat is transferred from the air to the aircraft skin. The maximum Mach number achievable before heat is transferred from the air to the skin is given by

$$\mathrm{Ma}_{\infty,\max} = \left[\frac{1}{r}\left(\frac{T_w}{T_\infty} - 1\right)\left(\frac{2}{\gamma - 1}\right)\right]^{1/2} \tag{2.23}$$

and is plotted in Figure 2.9 over a range of wall temperatures. The maximum Mach number increases with altitude and wall temperature. In Figure 2.10, the average convective heat transfer coefficient decreases monotonically with altitude due to the

continual decrease in the air density. In general, the convective heat transfer coefficient increases with Mach number, as expected. The average heat flux dissipated from the plate is shown in Figure 2.11. For low Mach numbers, the heat flux is positive for all values of altitude, which indicates that heat is transferred from the aircraft skin to the air. At high Mach numbers, however, the heat flux is negative at low altitudes due to the negative ΔT as shown in Figure 2.8. This means that the adiabatic wall temperature is higher than the skin temperature due to aerodynamic heating effects. The effect of heated plate length on the average heat flux for H = 0, 10, and 20 km is shown in Figure 2.12, Figure 2.13, and Figure 2.14. In general, the average heat flux decreases with plate length, and follows the behavior of the local heat transfer coefficient, where h_L is high at the leading edge and decreases as the boundary layer grows. Figure 2.15 shows the average heat flux dissipated over the plate versus altitude for the 1% hot day, the 1% cold day, and the standard atmosphere data as presented in Figure 2.1 and Figure 2.2. At low altitudes, q''_w is significantly higher for the 1% cold day due to the combined effects of the lower atmospheric temperature and the higher air density. The effect of wall temperature on average heat flux for a given airspeed is shown in Figure 2.16. The heat flux increases dramatically with altitude and wall temperature for low altitudes.

2.4 Conclusions

An analysis of the heat transfer from a heated plate has provided important insights for the possible use of the aircraft skin to reject heat from electric actuator systems. It was found that the altitude and speed of the aircraft significantly effected the amount of heat that could be rejected from the skin. Aerodynamic heating of the skin reduced the heat transfer, and if the Mach number was high enough, heat transfer from the skin to the air went to zero. A performance map of this phenomenon was provided. The altitude of the aircraft affected the freestream temperature and density, which in turn affected the overall heat transfer coefficient. It was also shown that assumption of a "standard atmosphere" could result in significant errors in the prediction of the heat dissipation as compared to the data for the 1% hot day or the 1% cold day. Finally, the analysis showed that the aircraft skin temperature, which is directly influenced by the

actuator thermal management system, has a strong effect on the heat dissipation rate, especially at low altitudes.

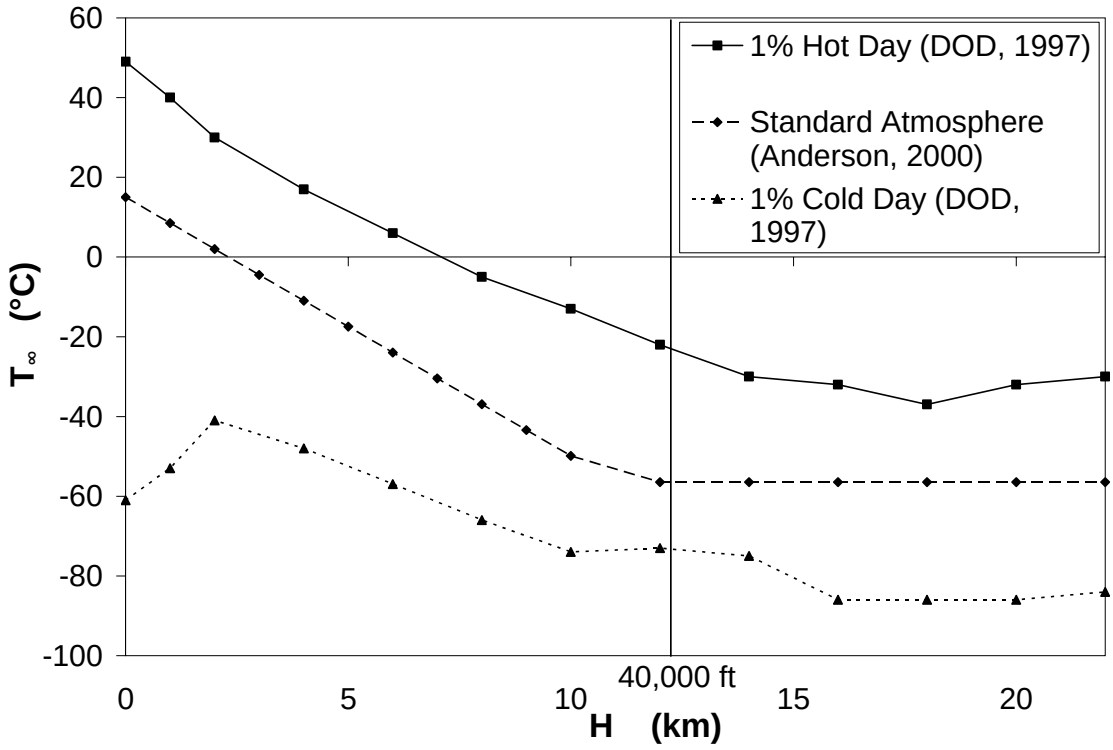

Figure 2.1. Atmospheric temperature versus altitude.

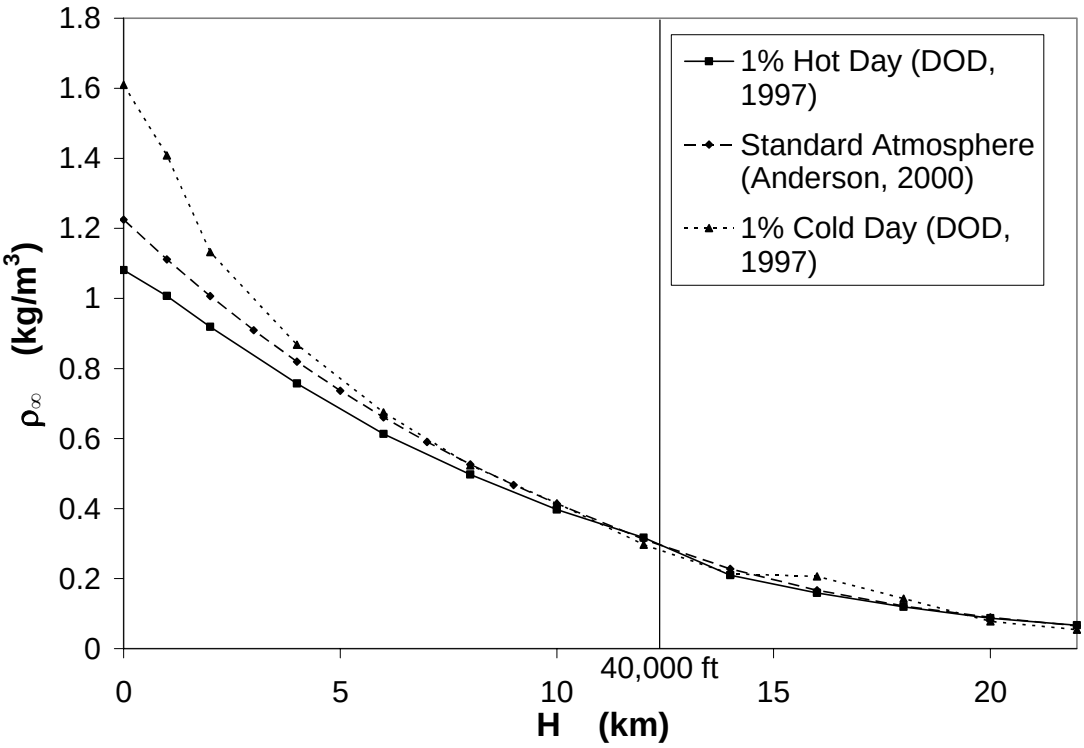

Figure 2.2. Atmospheric density versus altitude.

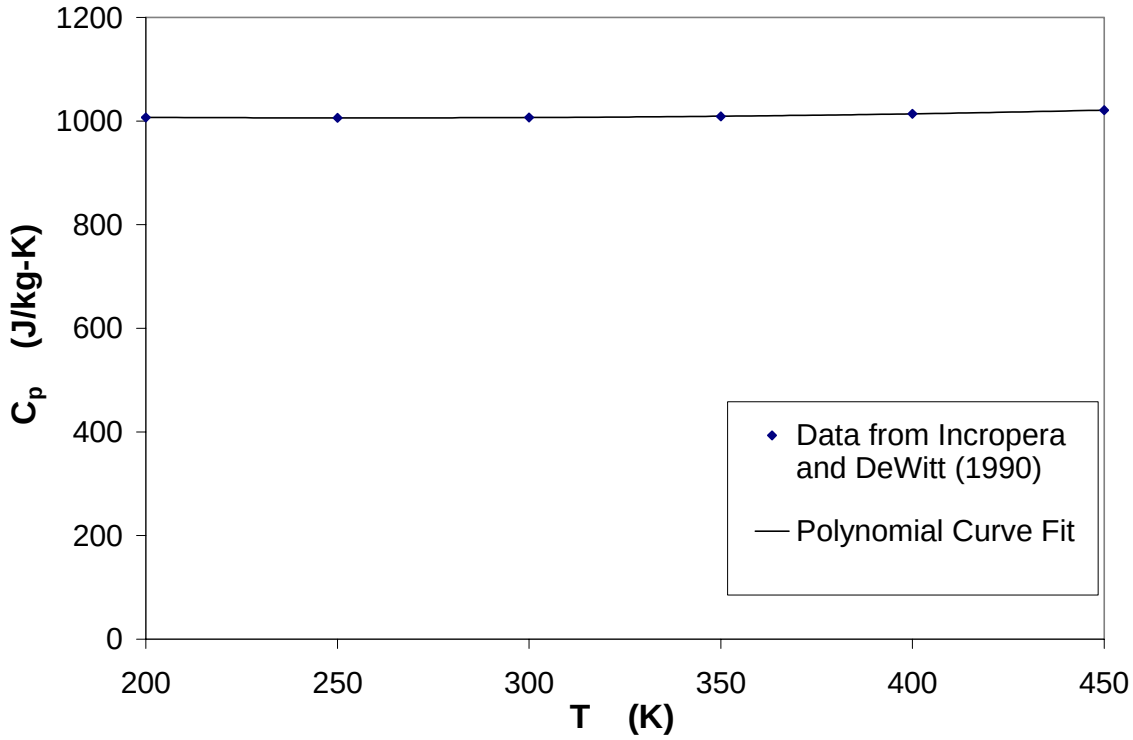

Figure 2.3. Specific heat of air versus temperature (Incropera and DeWitt, 1990).

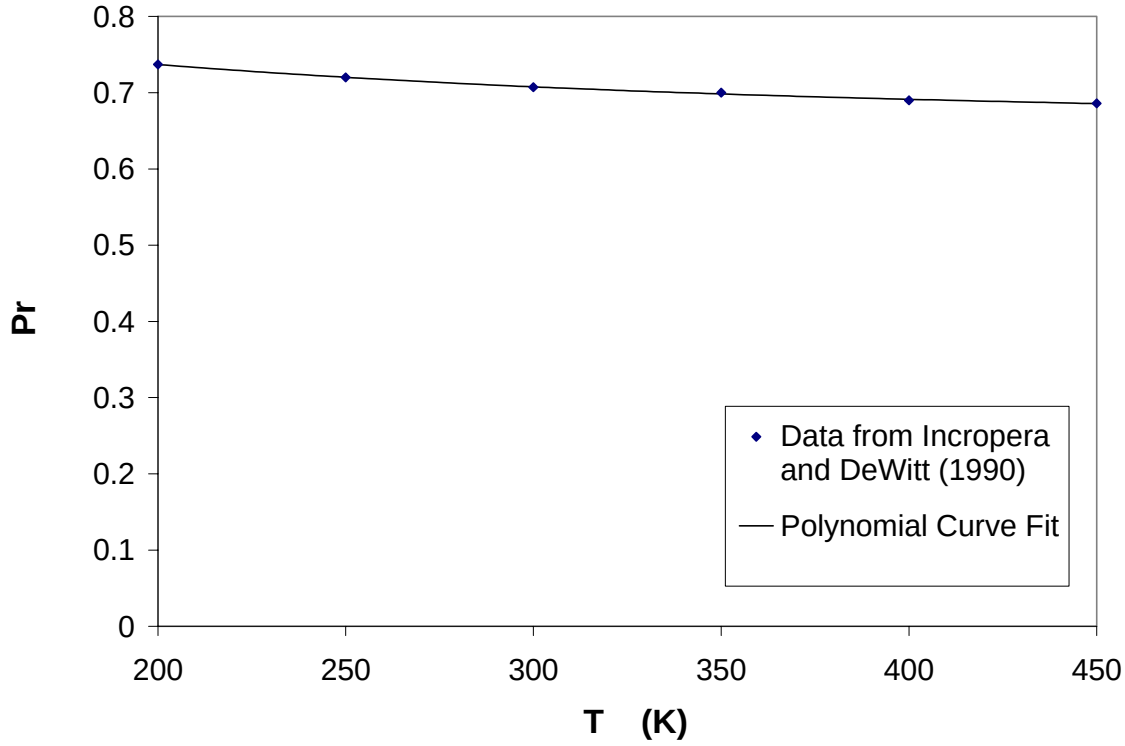

Figure 2.4. Prandtl number of air versus temperature (Incropera and DeWitt, 1990).

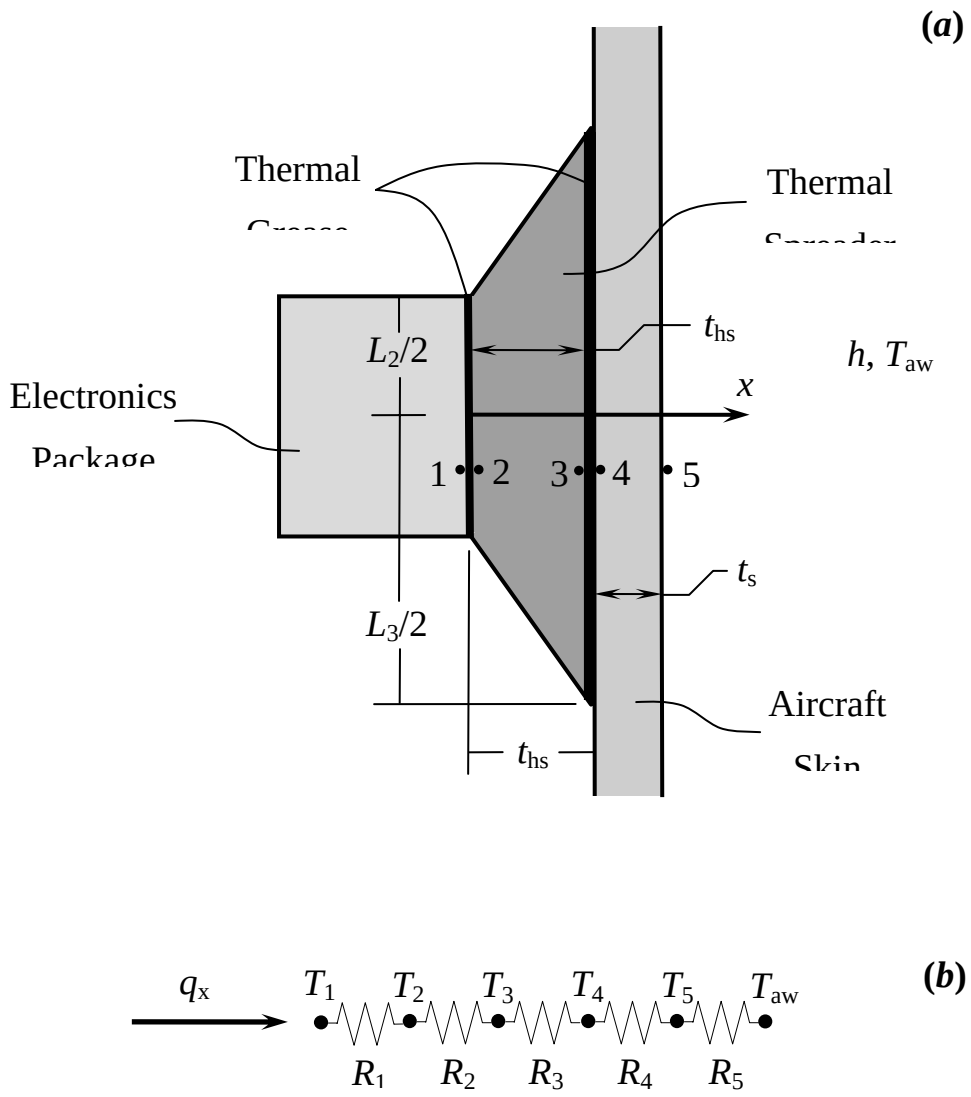

Figure 2.5. Schematic of direct mounting of the electronics package to the aircraft skin: (*a*) Geometric nomenclature; (*b*) Thermal resistance network.

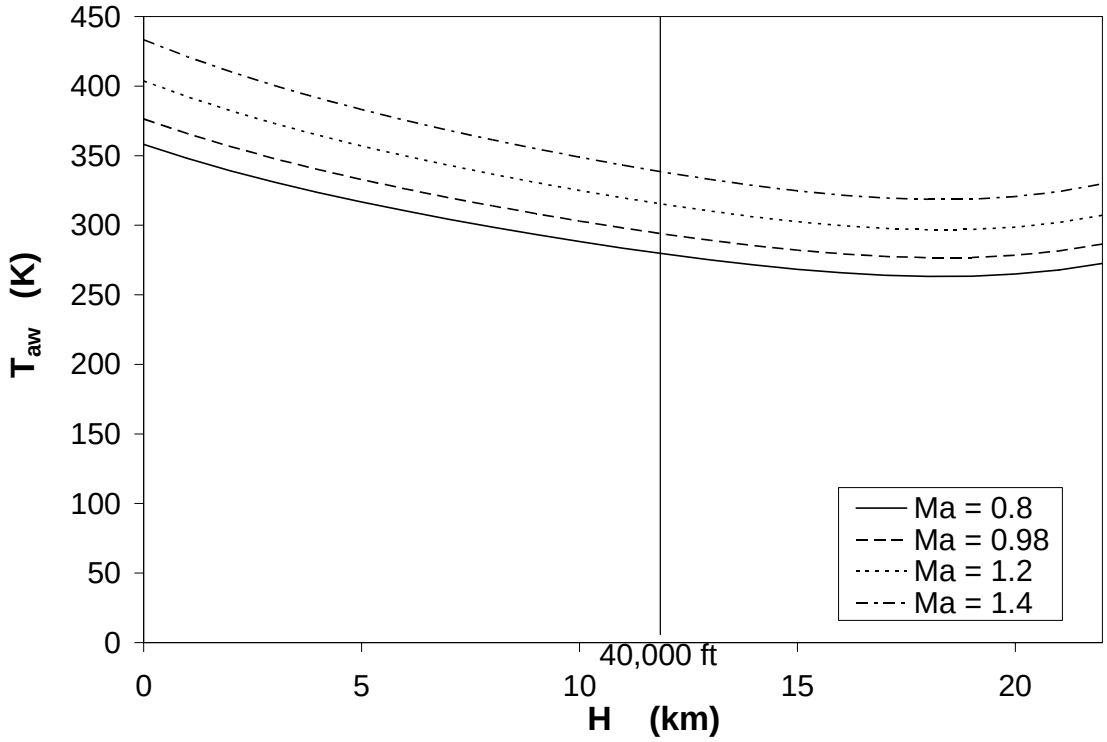

Figure 2.6. Adiabatic wall temperature versus altitude for various Mach numbers (1% hot day).

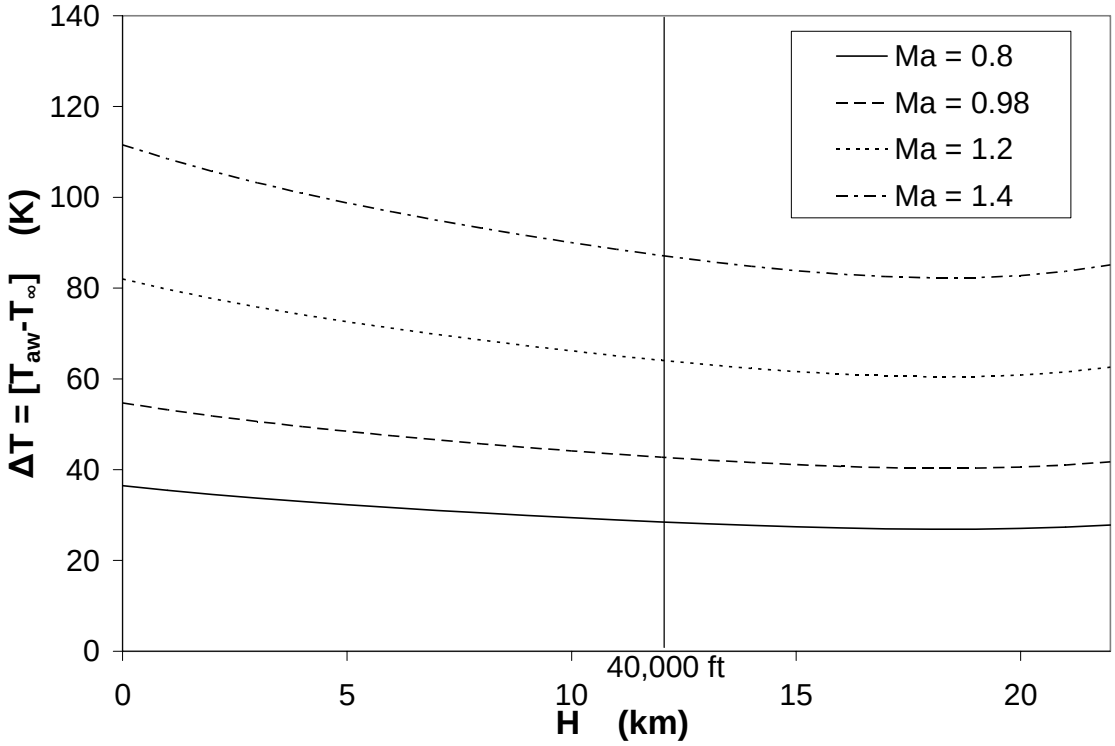

Figure 2.7. Temperature difference $(T_{\text{aw}} - T_{\infty})$ versus altitude for various Mach numbers (1% hot day).

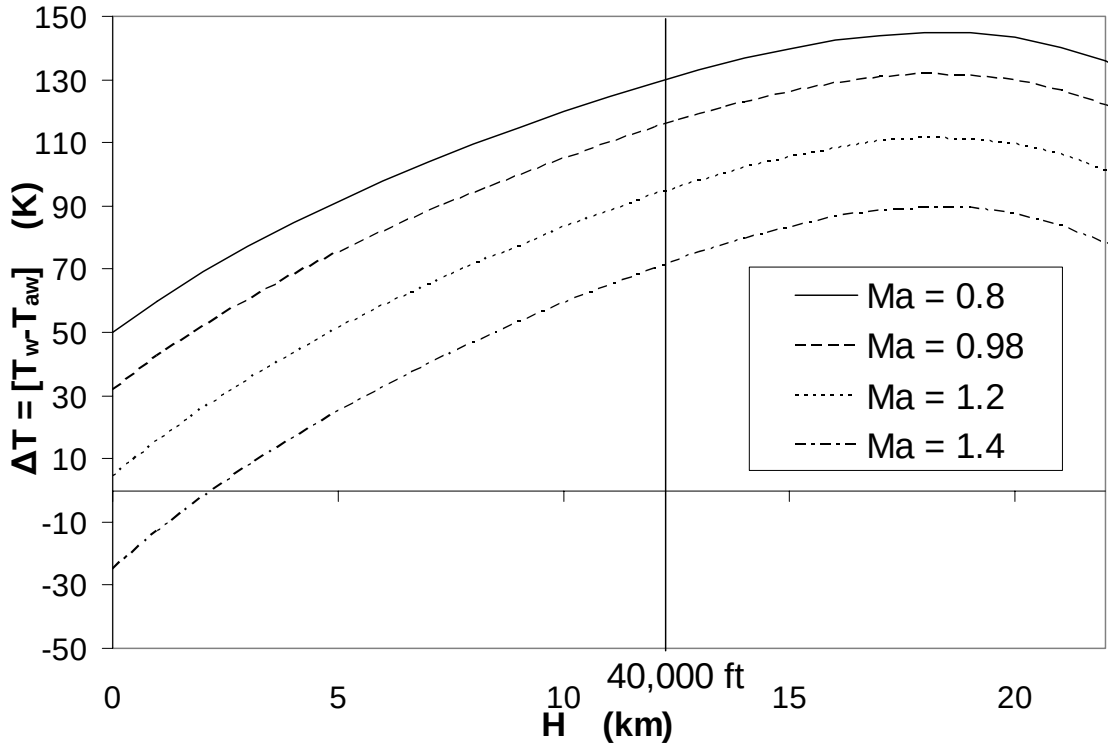

Figure 2.8. Temperature difference $(T_w - T_{aw})$ versus altitude for various Mach numbers (T_w = 135ºC, 1% hot day).

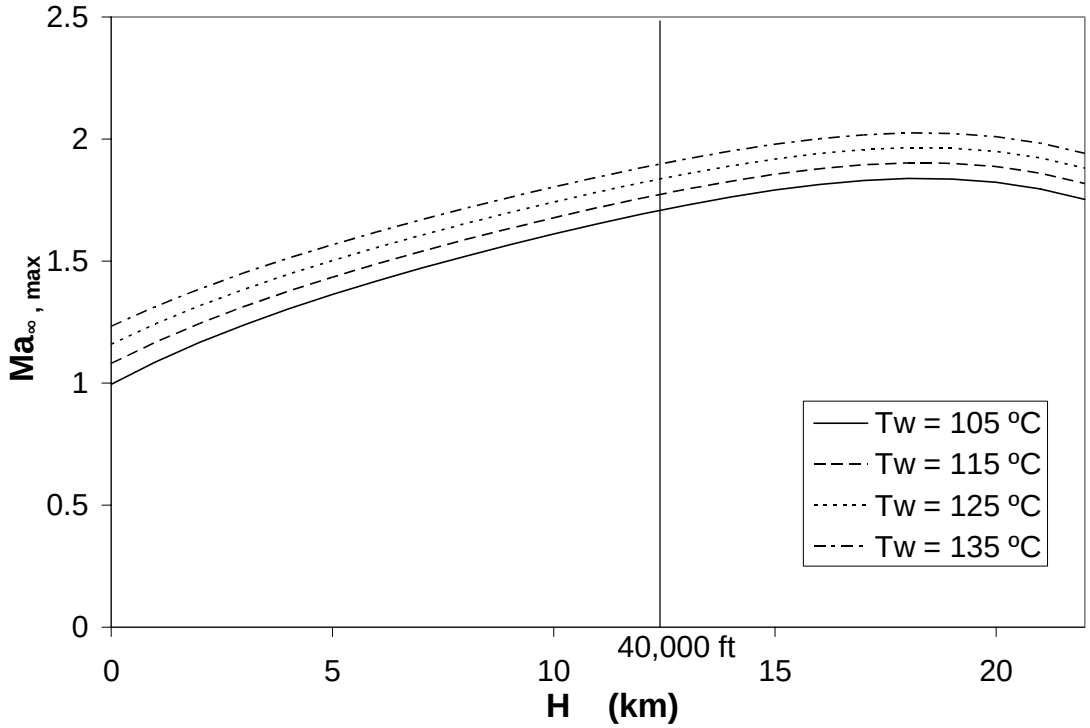

Figure 2.9. Maximum Mach number before heat is transferred from the air to the skin versus altitude for various wall temperatures (1% hot day).

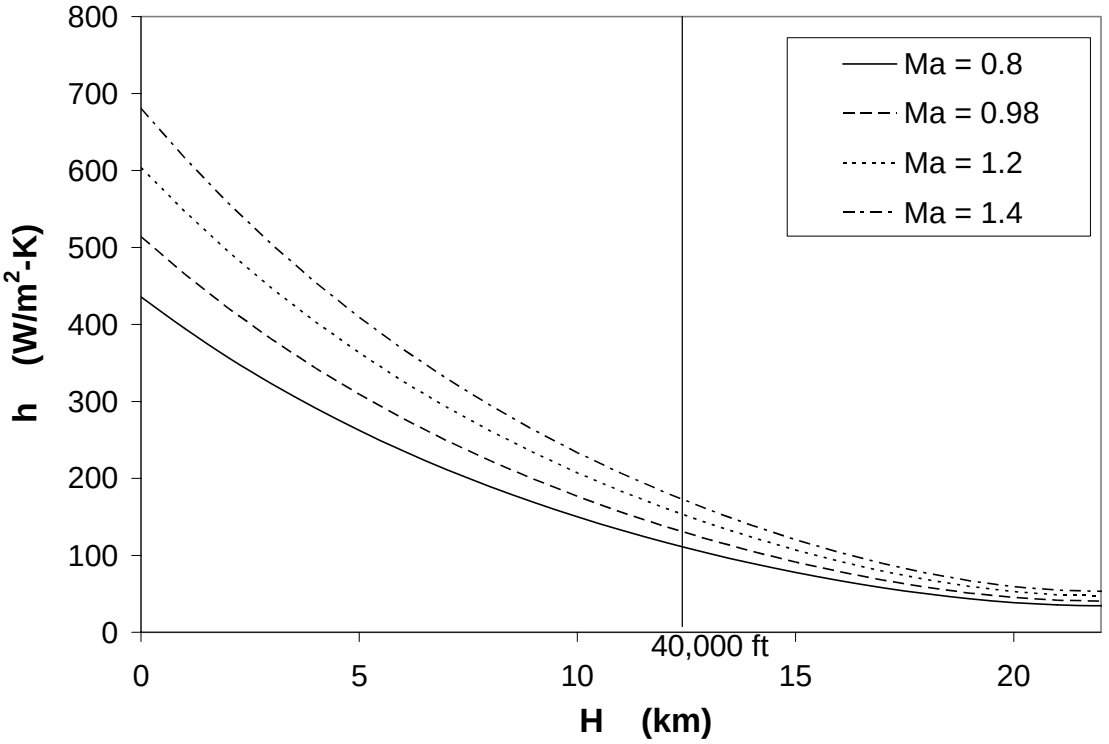

Figure 2.10. Average convective heat transfer coefficient versus altitude for various Mach numbers (T_w = 135ºC, L = 1.0 m, 1% hot day).

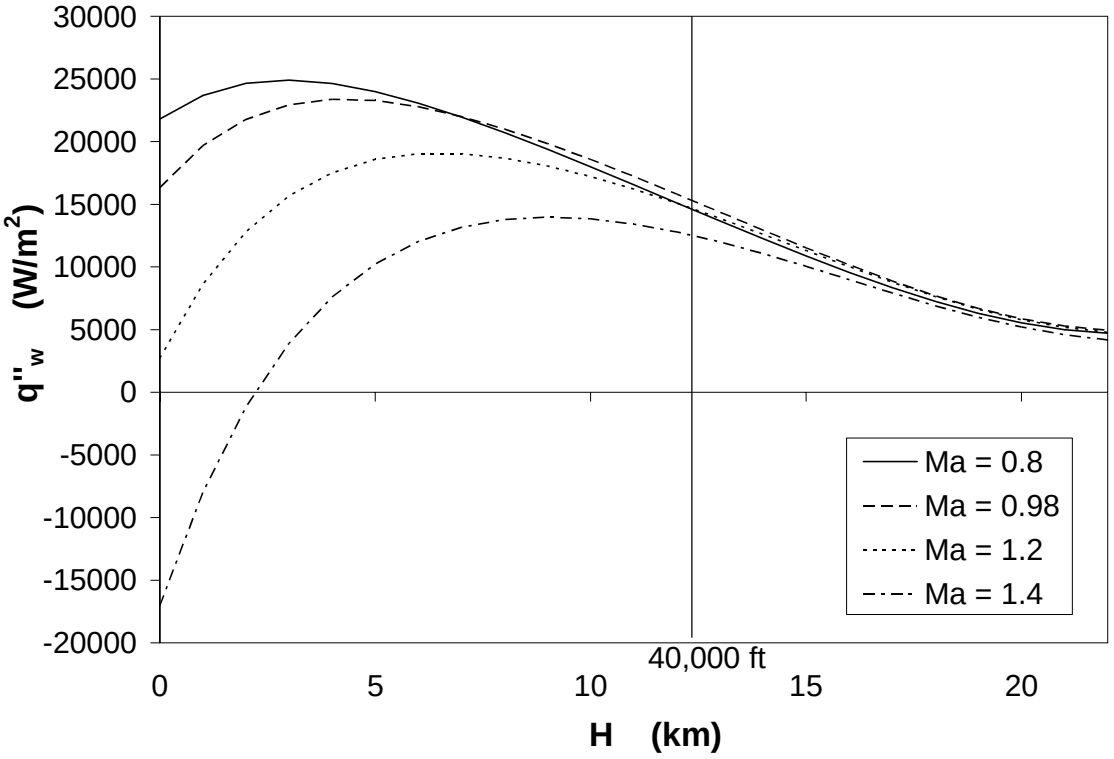

Figure 2.11. Average heat flux dissipated over the plate versus altitude for various Mach numbers (T_w = 135ºC, L = 1.0 m, 1% hot day).

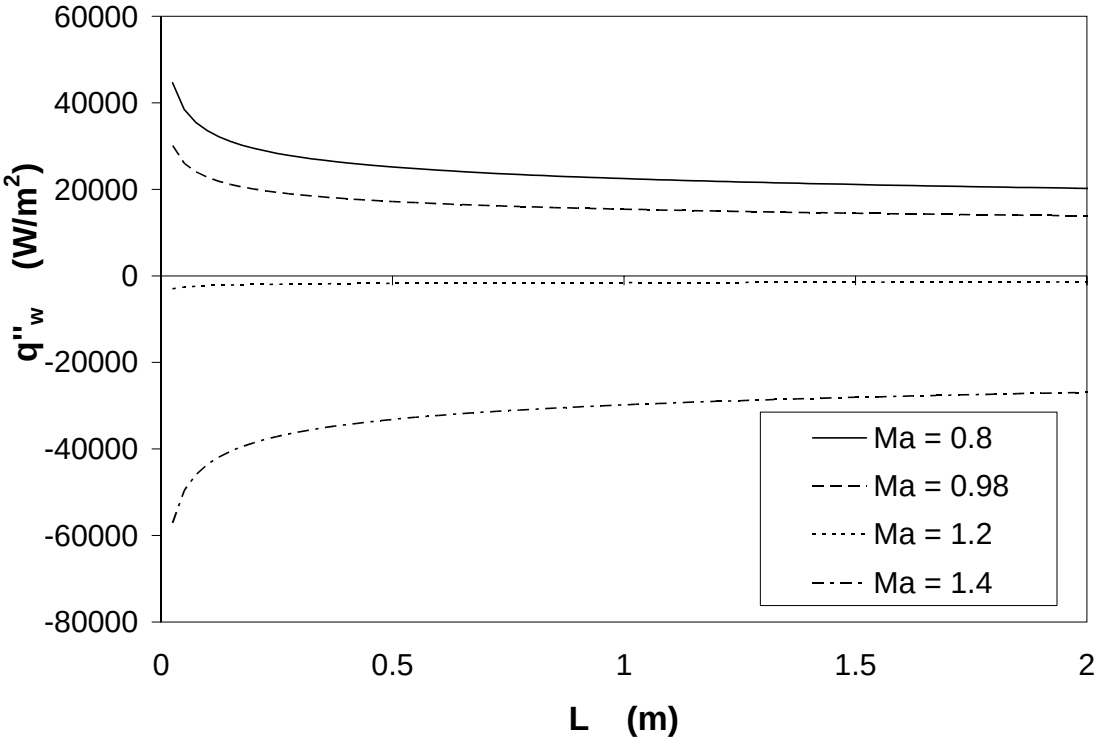

Figure 2.12. Average heat flux dissipated over the plate versus plate length for various Mach numbers (H = 0 km, T_w = 135ºC, 1% hot day).

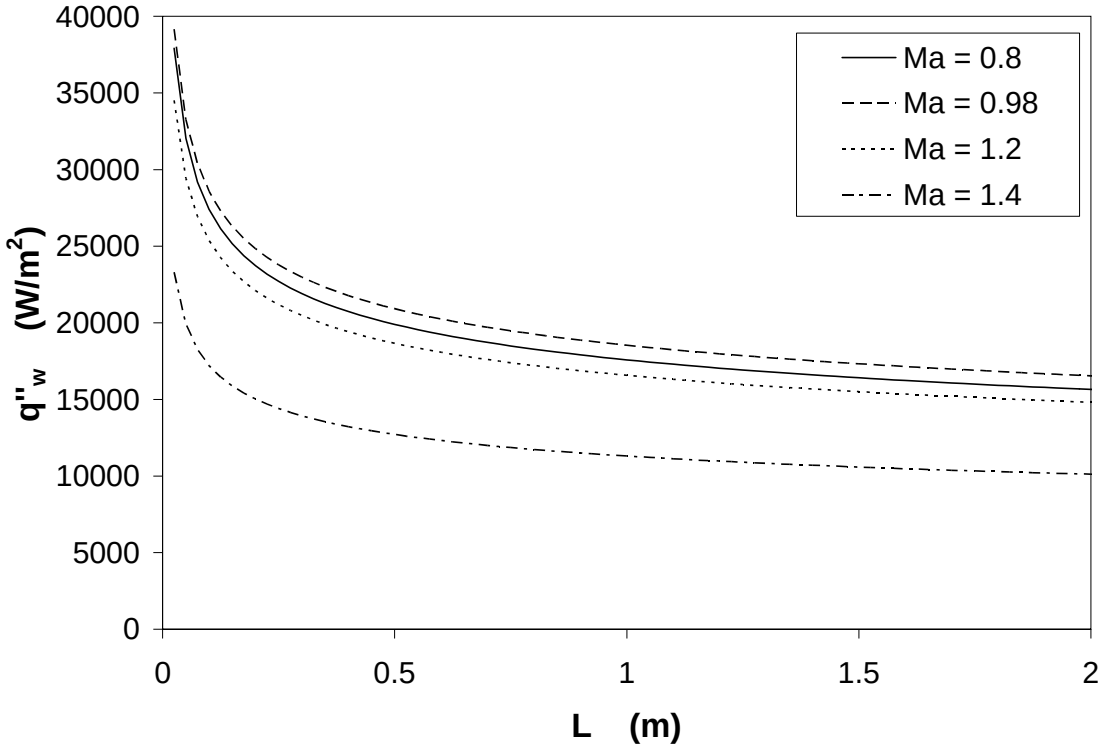

Figure 2.13. Average heat flux dissipated over the plate versus plate length for various Mach numbers (H = 10 km, T_w = 135ºC, 1% hot day).

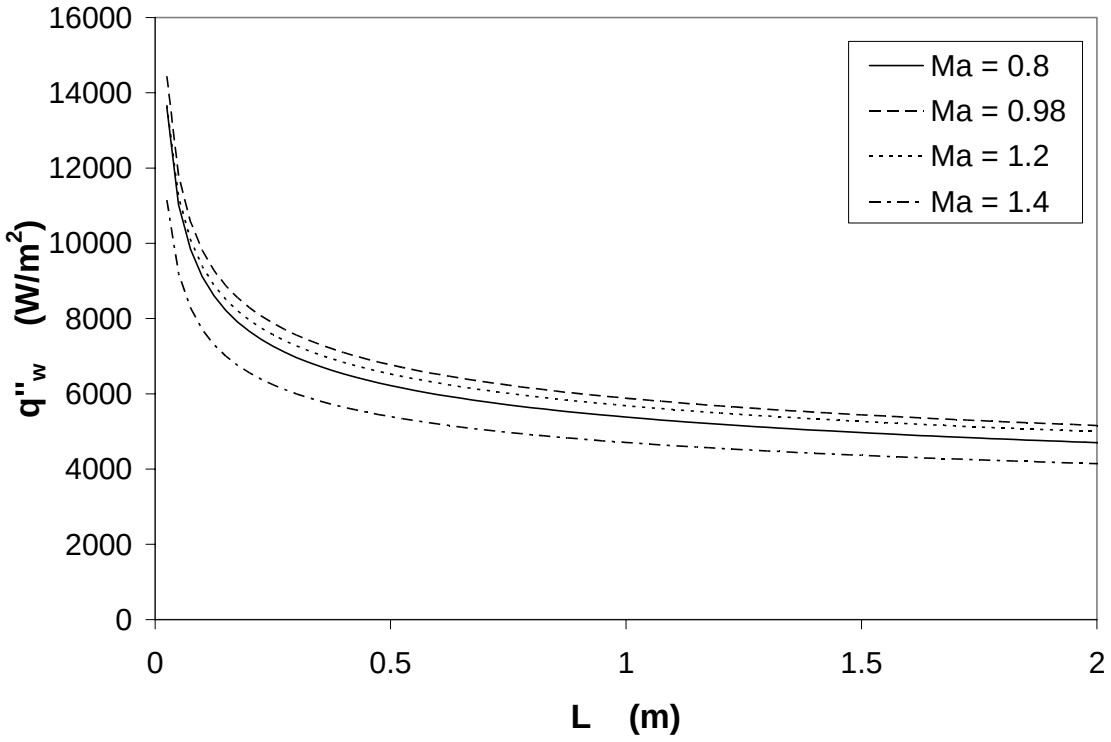

Figure 2.14. Average heat flux dissipated over the plate versus plate length for various Mach numbers (H = 20 km, T_w = 135ºC, 1% hot day).

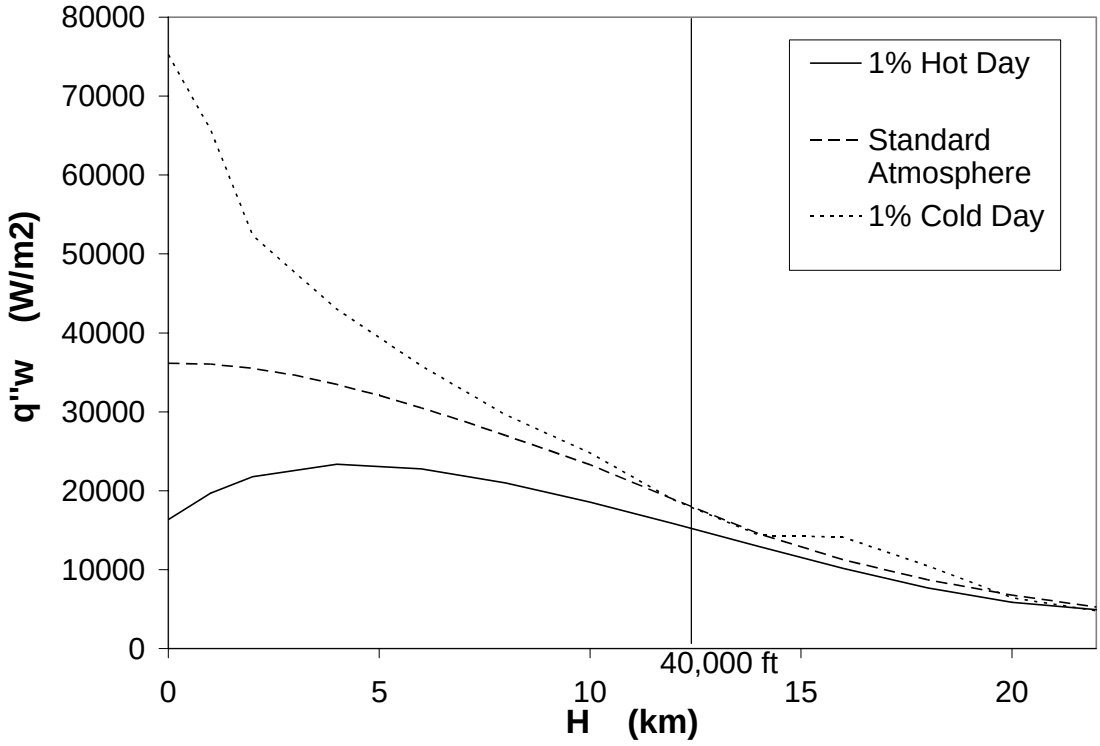

Figure 2.15. Average heat flux dissipated over the plate versus altitude for various atmospheric conditions (T_w = 135ºC, L = 1.0 m, Ma_∞ = 0.98).

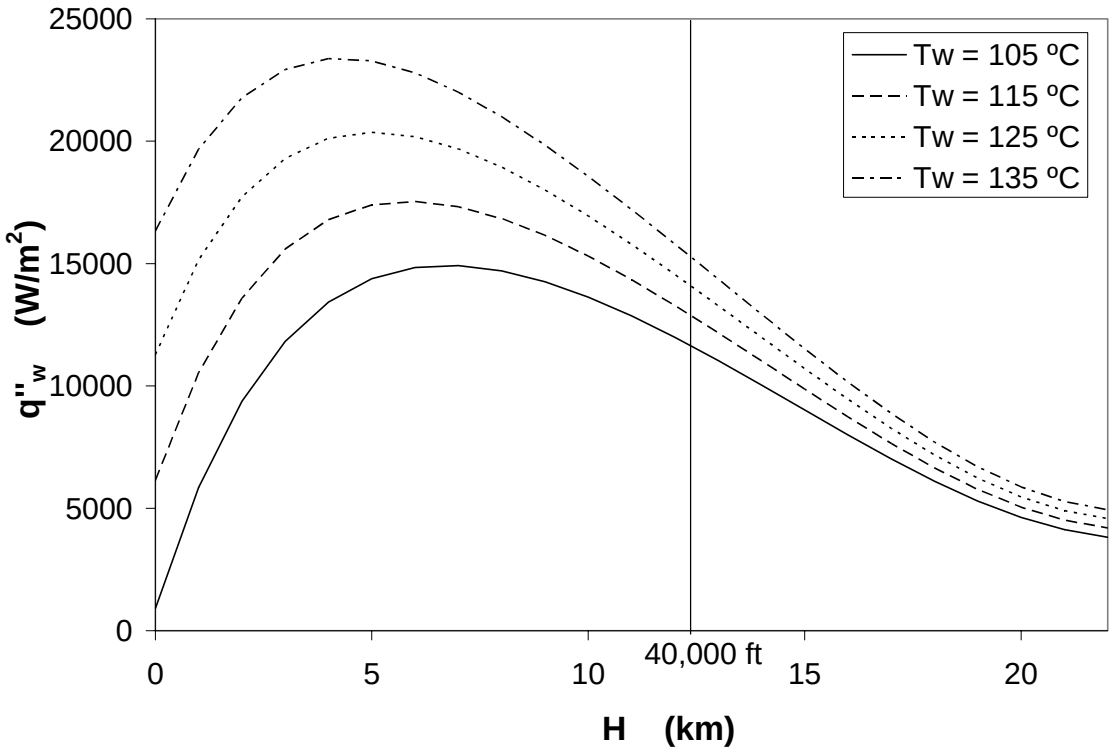

Figure 2.16. Average heat flux dissipation versus altitude for various wall temperatures ($Ma_\infty = 0.98$, $L = 1.0$ m, 1% hot day).

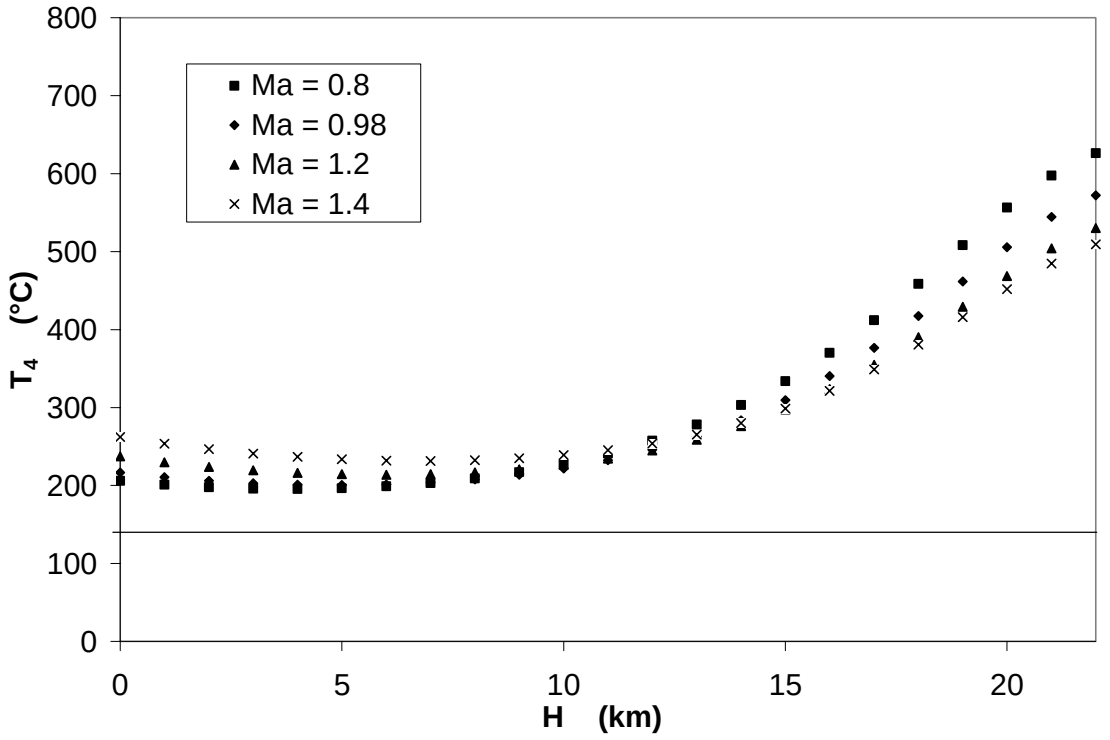

Figure 2.17. Maximum inner skin temperature versus altitude for various Mach numbers (1% hot day, $A = 204$ cm^2, $L = 14.28$ cm, $q_x = 500$ W, $R''_{t,c} = 0.9 \times 10^{-4}$ m^2-K/W)

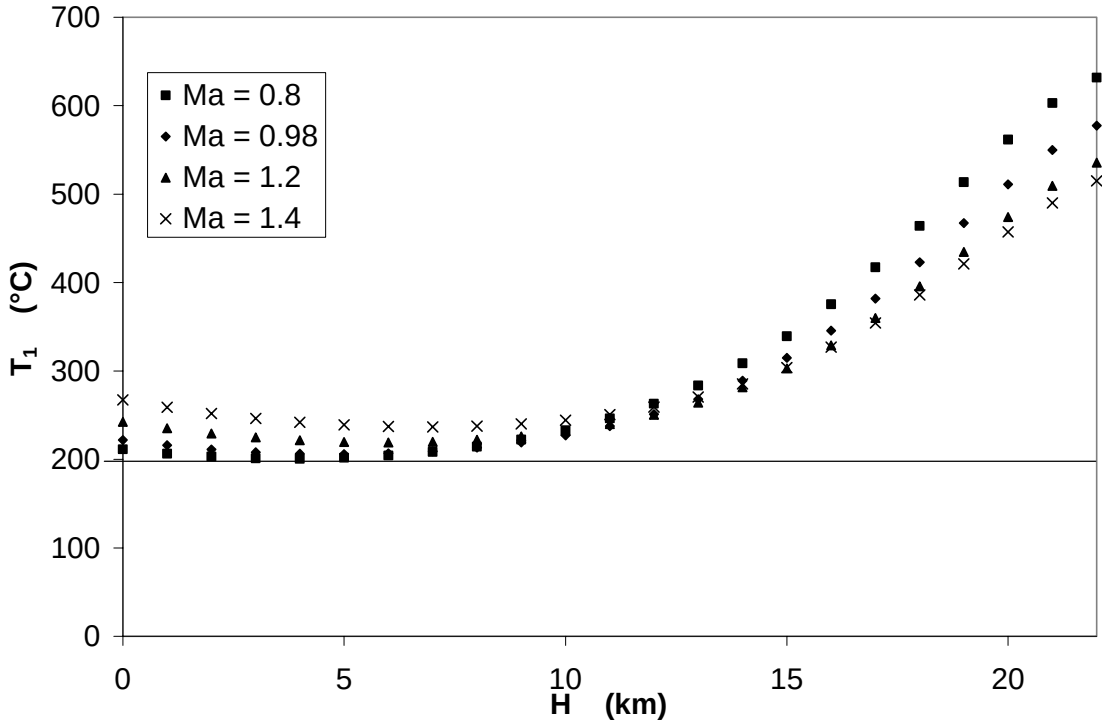

Figure 2.18. Maximum electronics unit edge temperature versus altitude for various Mach numbers (1% hot day, A = 166 cm^2, L = 12.88 cm, q_x = 500 W, $R''_{t,c} = 0.9\times10^{-4}$ m^2-K/W)

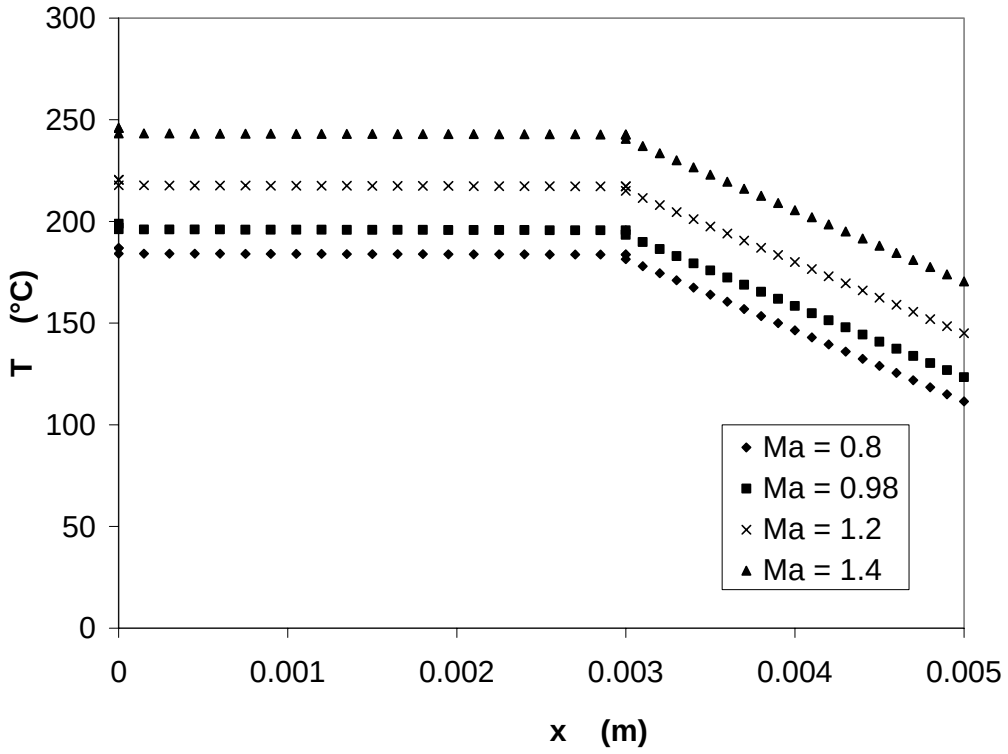

Figure 2.19. Temperature distribution through the aircraft skin for various Mach numbers (1% hot day, A_1 = 204 cm^2, A_2 = 166 cm^2, L = 12.88 cm, q_x = 500 W, $R''_{t,c} = 0.9 \times 10^{-4}$ m^2-K/W)

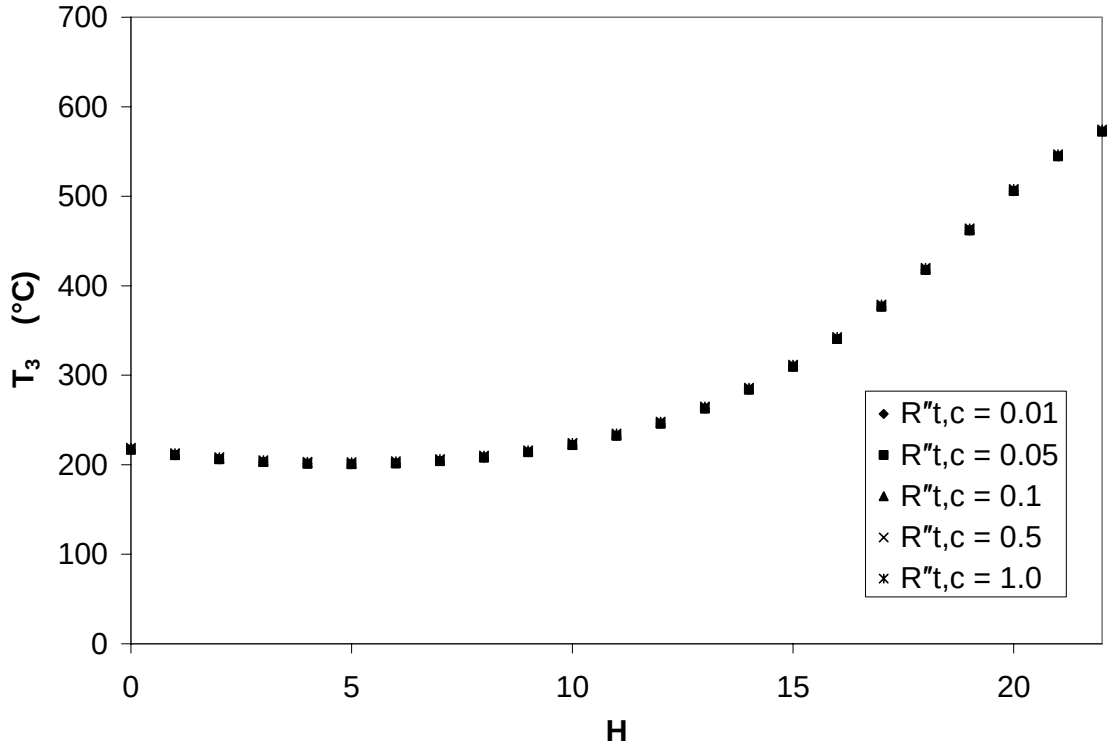

Figure 2.20. Outer-most face temperature of heat spreader versus altitude for various contact resistances (1% hot day, L_2 = 12.88 cm, L_3 = 14.28 cm, q_x = 500 W, k_{hs} = 0.7 W/m-K)

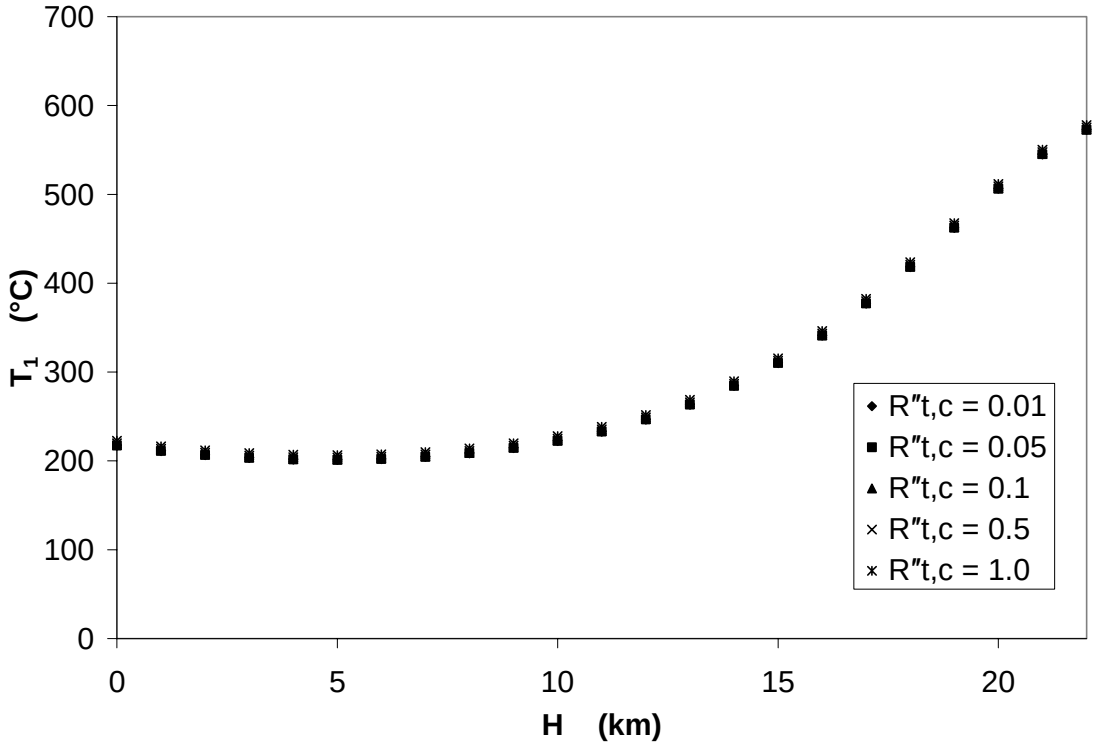

Figure 2.21. Electronics package temperature versus altitude for various contact resistances (1% hot day, $A = 166$ cm^2, $L_2 = 12.88$ cm, $q_x = 500$ W).

Table 2.1. Regression equations for air properties versus altitude for 1% hot day [from Table 5.3.1.1.2, DOD (1997)].

$$y = a_0 + a_1 H + a_2 H^2 + a_3 H^3 + a_4 H^4$$

[H in (km)]

Property	a_0	a_1	a_2	a_3	a_4	R^2
T_∞ (ºC)	4.8507E+1	-9.5033E+0	5.3483E-1	-2.8994E-2	7.7664E-4	0.99779
ρ_∞ (kg/m^3)	1.0868E+0	-8.9917E-2	2.0898E-3	-4.9336E-6	—	0.99954

Table 2.2. Regression equations for air properties versus temperature (Incropera and DeWitt, 1990).

$$y = a_0 + a_1 T + a_2 T^2 + a_3 T^3$$

[T in (K)]

Property	a_0	a_1	a_2	a_3	R^2
c_p (J/kg-K)	1.0187E+3	-6.9921E-2	-3.3333E-5	4.4444E-7	0.99916
Pr	8.6418E-1	-9.4177E-4	1.7778E-6	-1.2593E-9	0.99725

Table 2.3. Comparison of the present analysis with that presented by Leland (2004) (L = 1.0 m, T_w = 135ºC, 1% hot day).

Case 1: H = 0 kft, Ma_∞ = 0.98			
Value	Present analysis	Leland (2004)	% Difference
T_∞ (ºC)	48.51	49	-1.00
ρ_∞ (kg/m^3)	1.088	1.081	0.65
T_{aw} (°C)	103.8	104	-0.19
Re_L	1.94E+7	1.9E+7	1.89
T^*(°C)	103.8	104	-0.19
$\bar{h}$ (W/m^2-K)	513.6	506	1.51
$T_w - T_{aw}$ (°C)	31.78	31	2.52

Case 2: H = 5 kft, Ma_∞ = 0.98			
Value	Present analysis	Leland (2004)	% Difference
T_∞ (°C)	35.17	34	3.44
ρ_∞ (kg/m^3)	0.955	0.961	-0.62
T_{aw} (°C)	87.63	86	1.90
Re_L	1.74E+7	1.7E+7	2.35
T^* (°C)	96.63	96	0.66
$\bar{h}$ (W/m^2-K)	441.5	437	1.03
$T_w - T_{aw}$ (°C)	47.37	49	-3.33

Case 3: H = 40 kft, Ma_∞ = 1.4			
Value	Present analysis	Leland (2004)	% Difference
T_∞ (°C)	-23.24	-28	-17.00
ρ_∞ (kg/m^3)	0.295	0.307	-3.91
T_{aw} (°C)	63.68	58	9.79
Re_L	8.50E+6	8.4E+6	1.19
T^* (°C)	74.98	72	4.14
$\bar{h}$ (W/m^2-K)	177.4	179	-0.92
$T_w - T_{aw}$ (°C)	71.32	77	-7.38

Chapter 3: Future Directions

As previously stated, the objective of this project is to determine the suitability of using a loop heat pipe with water as the working fluid as a method of dissipating heat from electronics onboard aircraft. An analysis has been completed as outlined in Chapter 2 in which the heat transfer from a heated flat plate at zero angle of attack has been determined as a function of the altitude and speed of the aircraft, and the atmospheric weather conditions. This analysis will need to be coupled to the experimental setup on the centrifuge table with respect to the heat flux dissipated at the condenser section. On the centrifuge table, the condenser section will be mounted to a copper cold plate that will be cooled by a single-phase coolant loop. In order to quantify the heat transfer, accurate calorimetry will be required, which will necessitate very thorough calibration procedures for both the thermocouples and the flow meter. Difficulties are anticipated due to the fact that, in the past, significant noise levels were present in the thermocouple signals that were detected from the centrifuge table. A possible solution to this problem may be the use of coaxial cables from the stationary side of the slip rings to the data acquisition system in the control room. This method was recently used in order to successfully obtain video data from the rotating centrifuge table. Other possible solutions might include shielding the dc motor to reduce electro-magnetic field effects. The preliminary design of the high-temperature coolant loop will continue to be modified and refined. An initial objective here is to use an electric heater in order to simulate the heat transfer from the loop heat pipe. Proper operation of the high-temperature coolant loop will be verified, as well as the calibration procedures for the calorimeter as outlined above. In addition to the design of the high-temperature coolant loop, the design of the loop heat pipe itself will be initiated with respect to the sizes of the condenser and evaporator sections and interconnecting piping. This work will be done in cooperation with Dr. Jon Zuo of ACT. Limitations of the loop heat pipe will be discussed, and proper sizing of all components will be determined. Once the loop heat pipe is manufactured, it will be mounted to the centrifuge table and instrumented with thermocouples on the evaporator, condenser, compensation chamber and interconnecting tubing. Testing of the loop heat pipe will include steady state performance at normalized radial acceleration levels ranging from

$0.01 \le a_r^+ \le 9.0$. Transient testing of the loop heat pipe will require the purchase of additional equipment, as outlined previously. The radial acceleration and heat input to the loop heat pipe can be varied sinusoidally by using an arbitrary waveform generator with two channels. If purchased, this new equipment would have to be thoroughly integrated into the current data acquisition by creating and testing a new virtual instrument using LabVIEW. Once this has been accomplished, the loop heat pipe can be tested in a transient fashion by varying the frequency of the radial acceleration vector over a range that is of interest to AFRL that will simulate frequencies experienced during combat maneuvers. In addition, the frequency of the electrical heat input to the loop heat pipe could also be varied with or without a phase lag between the radial acceleration and the heat input. This would simulate the coupled behavior of the electric aircraft actuator that experiences a sudden spike in temperature and in acceleration during a typical maneuver.

In addition to the experimental work, several analytical models of the loop heat pipe thermal management system will be implemented. A model will be developed using ANSYS to analyze mounting an actuator directly to the aircraft skin. Since this may not be physically possible, another model will be developed using a loop heat pipe between the actuator and aircraft skin, using a heat spreader to mount the condenser to the aircraft skin. Of particular interest would be the infrared signature of the portion of the aircraft skin, which could be found using the numerical results of the study.

Figure 1.18 shows a projected timeline for the next ten months. Between now and December 2005, parts will be ordered for the high-temperature fluid loop. The loop will also be built and calibrated. A new LabVIEW VI will be written specifically for this experiment. When the loop heat pipe arrives, it will be implemented into the experimental setup. Experimentation will be conducted and then data reduction starting in January 2006. Along with experimentation, analytical models will be developed to compare results from experimentation.

Appendix A: Example Calculation of Average Heat Transfer Coefficient for Flat Plate Flow

Given:

Altitude: H = (5000 ft)(0.3048 m/ft) = 1524 m
Mach number: $Ma_\infty = 0.98$
Wall temperature: T_w = 135 °C = 408.15 K
Plate length: L = 1.0 m

Calculations:

Freestream temperature:
$T_\infty = (7.7664E\text{-}4)H^4 - (2.8994E\text{-}2)H^3 + (5.3483E\text{-}1)H^2 - (9.5033)H + (4.8507E+1)$
$T_\infty = 308.32$ K

Freestream density:
$\rho_\infty = (-4.9336E\text{-}6)H^3 + (2.0898E\text{-}3)H^2 - (8.9917E\text{-}2)H + 1.0868$
$\rho_\infty = 0.9550$ kg/m^3

Film temperature:
$T^* = T_\infty(0.5 + 0.039\ Ma_\infty^2) + 0.5T_w = (308.32\text{ K})(0.5+0.039(0.98)^2)+0.5(408.15\text{ K}) = 369.78$ K

Air density at the film temperature:
$\rho^* = \rho_\infty/(T_\infty/T^*) = (0.9550\text{ kg/m}^3)(308.32\text{ K})/(369.78\text{ K}) = 0.7963$ kg/m^3

Freestream speed of sound:
$a_\infty = \sqrt{(\gamma R T_\infty)} = \sqrt{((1.4)(286.9\text{ m}^2/\text{s}^2\cdot\text{K})(308.32\text{ K}))} = 351.9$ m/s

Freestream velocity:
$U_\infty = Ma_\infty a_\infty = (0.98)(351.9\text{ m/s}) = 344.87$ m/s

Freestream absolute viscosity (Reference values from Incropera and DeWitt, 1990):
$\mu_\infty = \mu_R(T_\infty/T_R)^{0.76} = (184.6 \times 10^{-7}\text{ N}\cdot\text{s/m}^2)(308.32\text{ K} / 300\text{ K})^{0.76} = 1.897 \times 10^{-5}$ N·s/m^2

Reynolds number:
$Re_L = (\rho_\infty U_\infty L)/\mu_\infty = (0.9550\text{ kg/m}^3)(344.87\text{ m/s})(1\text{ m}) / (1.897 \times 10^{-5}\text{ N}\cdot\text{s/m}^2) = 1.74 \times 10^7$
[TURBULENT]

Prandtl number at the film temperature:
$Pr^* = (-1.2593E\text{-}9)T^3 + (1.7778E\text{-}6)T^2 - (9.4177E\text{-}4)T + (8.6418E\text{-}1)$
$Pr^* = 0.6954$

Specific heat at the film temperature:

$c_p^* = (4.4444\text{E-}7)T^3 - (3.3333\text{E-}5)T^2 - (6.9921\text{E-}2)T + (1.0187\text{E+}3)$
$c_p^* = 1010.76$ J/(kg·K)

Recovery factor for turbulent flow:
$r = \text{Pr}^{*1/3} = (0.6954)^{1/3} = 0.8860$

Adiabatic wall temperature:
$T_{aw} = T_\infty[1+r((\gamma\text{-}1)/2)\text{Ma}_\infty^2] = (308.32\text{ K})(1+(0.8860)(0.4/2)(0.98)^2) = 360.8$ K

Absolute viscosity at the film temperature:
$\mu^* = \mu_R(T^*/T_R)^{0.76} = (184.6 \times 10^{-7}\text{ N}\cdot\text{ s/m}^2)(369.78\text{ K} / 300\text{ K})^{0.76} = 2.275 \times 10^{-5}$ N·s/m^2

Local skin friction coefficient at the end of the plate:
$C_{f,L}^* = 0.455/(\ln^2(0.06\rho^* U_\infty L/ \mu^*))$
$= 0.455/(\ln^2(0.06(0.7963\text{ kg/m}^3)(344.87\text{ m/s})(1\text{ m}) / (2.275 \times 10^{-5}\text{ N}\cdot\text{ s/m}^2))$
$= 0.002499$

Local Stanton number at the end of the plate:
$\text{St}_L^* = (C_{f,L}^*/2) / (1+12.7(\text{Pr}^{*2/3}\text{-}1)(C_{f,L}^*/2)^{1/2}$
$= (0.002499/2) / (1+12.7((0.6954)^{2/3}\text{-}1)(0.002499/2)^{1/2}) = 0.001383$

Local heat transfer coefficient at the end of the plate:
$h_L = \text{St}_L^* \rho^* U_\infty c_p^* = (0.001383)(0.7963\text{ kg/m}^3)(344.87\text{ m/s})(1010.76\text{ J/kg}\cdot\text{K})$
$= 383.9$ W/m^2·K

Average heat transfer coefficient over the length of the plate:
$\bar{h} = 1.15\, h_L = 1.15(383.9\text{ W/m}^2\cdot\text{K}) = 441.52$ W/m^2·K

Average heat flux dissipated over the plate:
$q''_w = \bar{h}(T_w - T_{aw}) = (441.52\text{ W/m}^2\cdot\text{K})(408.15\text{ K} - 360.8\text{ K}) = 20913.13$ W/m^2

Appendix B: Example Calculation of Temperature Distribution for Direct Mounting of Electronic Unit to Aircraft Skin

Given:

Altitude, H	(5000 ft) (0.3048 m/ft) = 1524 m
Mach number, Ma_∞	0.98
Plate length on skin, L_3	0.1428 m
Length of electronic unit, L_2	0.1288 m
Skin thickness, t_s	(0.08 in)(0.0254 m/in) = 0.002032 m
Contact resistance, $R_c^{"}$	0.9×10^{-4} m^2-K/W
Heat rate, q_x	500 W

Freestream temperature:
$T_\infty = (7.7664E\text{-}4)H^4 - (2.8994E\text{-}2)H^3 + (5.3483E\text{-}1)H^2 - (9.5033)H + (4.8507E+1)$
$T_\infty = 308.3$ K

Freestream density:
$\rho_\infty = (-4.9336E\text{-}6)H^3 + (2.0898E\text{-}3)H^2 - (8.9917E\text{-}2)H + 1.0868$
$\rho_\infty = 0.9546$ kg/m^3

Freestream speed of sound:
$a_\infty = \sqrt{(\gamma R T_\infty)} = \sqrt{((1.4)(286.9\ m^2/s^2\text{-K})(308.3\ K))} = 351.97$ m/s

Freestream velocity:
$U_\infty = Ma_\infty\, a_\infty = (0.98)(351.9\ m/s) = 344.93$ m/s

Freestream absolute viscosity (Reference values from Incropera and DeWitt, 1990):
$\mu_\infty = \mu_R(T_\infty/T_R)^{0.76} = (184.6 \times 10^{-7}\ N\cdot s/m^2)(308.3\ K / 300\ K)^{0.76} = 1.897 \times 10^{-5}\ N\cdot s/m^2$

Reynolds number:
$Re_L = (\rho_\infty U_\infty L)/\mu_\infty = (0.9550\ kg/m^3)(344.9\ m/s)(1\ m) / (1.897 \times 10^{-5}\ N\cdot s/m^2) = 1.74 \times 10^7$
[TURBULENT]

The following formulas were solved iteratively due to dependence the film properties on the wall temperature:

Film temperature:
$T^* = T_\infty (0.5 + 0.039\ Ma_\infty^2) + 0.5T_5$

Prandtl number at the film temperature:
$Pr^* = (-1.2593E\text{-}9)T^3 + (1.7778E\text{-}6)T^2 - (9.4177E\text{-}4)T + (8.6418E\text{-}1)$

Recovery factor for turbulent flow:
$r = \mathrm{Pr}^{*1/3}$

Specific heat at the film temperature:
$c_p^* = (4.4444\text{E-}7)T^3 - (3.3333\text{E-}5)T^2 - (6.9921\text{E-}2)T + (1.0187\text{E+}3)$

Absolute viscosity at the film temperature:
$\mu^* = \mu_R(T^*/T_R)^{0.76}$

Adiabatic wall temperature:
$T_{aw} = T_\infty[1+r((\gamma\text{-}1)/2)\mathrm{Ma}_\infty^2]$

Skin Temperature:
$T_5 = q_x / (\bar{h} \cdot L_3^2) + T_{aw}$

Air density at the film temperature:
$\rho^* = \rho_\infty / (T_\infty / T^*)$

Local skin friction coefficient at the end of the plate:
$C_{f,L}* = 0.455 / (\ln^2(0.06\, \rho^* U_\infty L / \mu^*))$

Local Stanton number at the end of the plate:
$\mathrm{St}_L^* = (C_{f,L}^*/2) / (1+12.7(\mathrm{Pr}^{*2/3} - 1)(C_{f,L}^*/2)^{1/2}$

Local heat transfer coefficient at the end of the plate:
$h_L = St_L^* \rho^* U_\infty c_p^*$

Average heat transfer coefficient over the length of the plate:
$\bar{h} = 1.15\, h_L$

The above system of equations was solved iteratively, and the values found are:
$T^* = 364.0$ K
$\mathrm{Pr}^* = 0.6962$
$c_p^* = 1007$ J/kg·K
$\mu^* = 3.920 \times 10^{-5}$ N·s/m^2
$r = 0.8863$
$T_{aw} = 360.8$ K
$T_5 = 396.5$ K
$C_{f,L}^* = 0.003748$
$\mathrm{St}_L^* = 0.002124$
$h_L = 596.72$ W/m^2·K
$\bar{h} = 686.23$ W/ m^2·K

Inner skin temperature:
$T_4 = T_5 + (q_x \cdot t_s) / (k_s \cdot L_s^2) = 396.52$ K + (500 W)(0.002 m) /[(0.7 W/m·K)(0.0204 m^2)]

T_4 = 466.55 K

Temperature of the outer face of heat spreader:
$T_3 = T_4 + q_x \cdot R''_{t,c} / L_3^2$ = 466.5 K + (500 W · 0.9 x 10^{-4} m^2·K/W) / (0.1428 m)^2
T_3 = 468.8 K

Temperature of the inner face of heat spreader:

$$T_2 = T_3 + \frac{q_x}{k_{hs}\sqrt{ab}} \cdot \tan^{-1}\left(\frac{t_{hs}\sqrt{ab}}{b}\right)$$

where

$$a = \frac{L_3^2 - L_2^2}{t_{hs}^2}, \quad b = L_2^2$$

$$a = \frac{(0.1428\ \text{m})^2 - (0.1288\ \text{m})^2}{(0.003\ \text{m})^2} = 422.49, \quad b = (0.1288\ \text{m})^2 = 0.016589\ \text{m}^2$$

$$T_2 = (468.8\ \text{K}) + \frac{(500\ \text{W})}{(177\ \text{W/m}\cdot\text{K})\sqrt{(422.49)(0.1288\ \text{m})^2}} \cdot \tan^{-1}\left(\frac{(0.003\ \text{m})\sqrt{(422.49)(0.016589\ \text{m}^2)}}{(0.016589\ \text{m}^2)}\right)$$

T_2 = 469.2 K

Temperature of the edge of the electronics package:
$T_1 = T_2 + q_x\, R''_{t,c} / L_2^2$ = 469.2 K + 500 W · 0.9 x 10^{-4} m^2-K/W / (0.1288 m)^2
T_1 = 471.9 K

References

F. Incropera and D. DeWitt, 1990, *Fundamentals of Heat and Mass Transfer,* Third edn., Wiley, New York.

F. White, 1988, *Heat and Mass Transfer,* Addison-Wesley, New York.

NACA, 1953, *Equations, Tables, and Charts for Compressible Flow,* NACA Report 1135, U.S. Government Printing Office, Washington, D.C.

DOD, 1997, *Global Climatic Data for Developing Military Products,* Department of Defense Handbook, MIL-HDBK-310.

Q. Leland, 2004, personal communication.

J. Anderson, 2000, *Introduction to Flight,* Fourth edn., McGraw-Hill, Boston.